Radiometric Noise Assessment of the Cross-track Infrared Sounder on the NOAA-20 Satellite

Denis A. Tremblay, F. Iturbide-Sanchez, Y. Chen, L. Borg, J. Predina, X. Jin, D. Tobin, L. Strow, D. Mooney, D. Johnson, L. Suwinski, and H. Revercomb

Abstract—**The Cross-track Infrared Sounder (CrIS) is a Michelson-type Fourier Transform Spectrometer. The CrIS flight module 2 instrument was launched into orbit on 18 November 2017 onboard the NOAA-20 satellite as part of the United States (US) Joint Polar Satellite System (JPSS). The CrIS instrument measures the top-of-atmosphere upwelling spectral radiance in the thermal infrared (IR) spectrum. These measurements provide critical information for medium range weather forecasting, and for the retrieval of atmospheric profiles of temperature, water vapor, and other trace gases. The instrument noise equivalent radiance differential (NEdN) estimates are used by the weather forecasting systems, the trace gas atmospheric retrieval algorithms, and for trending the health and stability of the instrument over time. The current operational NEdN estimate is calculated using instrument observations from the Deep Space (DS) view and the Internal Calibration Target (ICT). Two alternative methodologies are described here based on the principal component analysis (PCA) of an ensemble of calibrated Earth scene spectra. The NEdN calculation methods show that the instrument meets the specifications with margin for all 27 detectors with the exception of one mid-wave infrared (MWIR) field-of-view (FOV) 9, which is borderline. The PCA analysis shows that warmer Earth scene spectra have higher noise, known as scene shot, for the short-wave infrared (SWIR) band. Using the PCA analysis, the NEdN for the long-wave IR FOV 5 is 30% higher than the NEdN calculated by the operational algorithm. Correlated noise is also found due to the effect of the instrument self-apodization correction.**

***Index Terms*—Calibration, CrIS, NOAA-20 Satellite, Noise Estimates**

I. Introduction

The Cross-track Infrared Sounder (CrIS) flight module 2 (FM2) onboard the NOAA-20 satellite is a Michelson Fourier Transform Spectrometer (FTS). The noise equivalent spectral radiance differential (NEdN) estimates of each CrIS spectral channel is an intrinsic part of the apriori information [1, 2, 3] assimilated into weather forecasting models [4] for the purpose of retrieving the atmospheric vertical profiles of trace gases.

CrIS FM2 was launched into orbit on 18 November 2017 onboard the NOAA-20 satellite. Starting with FM1 that is currently flying onboard the Suomi National Polar-orbital Partnership (S-NPP) satellite, FM2 is the second in a series of five CrIS instruments where FM3 to FM5 are planned for launch from 2022 to 2031 on JPSS-2, JPSS-3 and JPSS-4 satellites respectively. The CrIS instrument uses three infrared focal planes each measuring the top-of-atmosphere spectral radiance covering three distinct spectral bands. The infrared spectral bands are the long wavelength infrared or LWIR (650 to 1095 cm^{-1}), the mid wavelength infrared or MWIR (1210 to 1750 cm^{-1}) and the short wavelength infrared or SWIR (2155 to 2550 cm^{-1}). The scene selection module (SSM) is the upfront

This paragraph of the first footnote will contain the date on which you submitted your paper for review. It will also contain support information, including sponsor and financial support acknowledgment. For example, "This work was supported in part by the U.S. Department of Commerce under Grant BS123456." This work was supported by the National Oceanic and Atmospheric Administration under contract ST133017CQ0050. (Corresponding author: Denis Tremblay)

D. Tremblay and X. Jin are with Global Science Technology Inc., Greenbelt, MD 20770 USA (email: denis.tremblay@noaa.gov, xin.jin@noaa.gov)

L. Borg, D. Tobin, H. Revercomb are with the University of Wisconsin-Madison, Madison, Wisconsin, USA 53706 (email: lori.borg@ssec.wisc.edu, dave.tobin@ssec.wisc.edu, hank.revercomb@ssec.wisc.edu)

F. Iturbide-Sanchez and Y. Chen are with the National Oceanic and Atmospheric Administration (NOAA), College Park, MD 20740 USA (email: Flavio.iturbide@noaa.gov, yong.chen@noaa.gov)

J. Predina is with Logistikos LLC, Fort Wayne Indiana, Indiana, USA 46845 (email: joe.predina@logistikosengineering.com)

L. Strow is with the University of Maryland Baltimore County (UMBC), physics department, Baltimore, MD 21250 (email: strow@umbc.edu)

D. Mooney is with the Massachusetts Institute of Technology (MIT) affiliated with the Lincoln Laboratory, Lexington, MA, USA 02420 (email: mooney@ll.mit.edu)

D. Johnson is with NASA Langley Research Center, Hampton, Virginia, USA, 23581 (email: david.g.johnson@nasa.gov).

L. Suwinski is with L3Harris corporation, Fort Wayne, Indiana, USA, 46825 (email: Lawrence.suwinski@l3harris.com)

pivoting mirror that allows the measurements to be taken at different cross-track scanning angles. It takes 8 seconds to acquire one full scan that comprises 34 fields-of-regard (FOR). The FOR 1 to 30 view the Earth scenes that have a cross-track angles ranging from -48 to + 48 degrees with respect to the nadir. The remaining four FORs acquire the calibration measurements of the internal calibration target (ICT), a hot black body cavity, and the deep space (DS) view for each of the two mirror sweep directions. One cross-track scan covers a 2100 km swath on the Earth surface. For each of the three focal planes, the nine detector circular field stops form a 3 by 3 grid array giving nine fields-of-view (FOV). At nadir, a single FOV projects a 14 km diameter footprint on the Earth surface. The CrIS data acquisition pattern and Sensor Data Record (SDR or Level 1B) product information can be found in the CrIS user's guide [5].

The Interface Data Processing System (IDPS) performs the operational ground data processing. Two ground receiving stations acquire the Raw Data Record (RDR or Level 0 data). The RDR contains the compressed interferogram measurements and are transmitted to the NOAA Satellite Operation Facility (NSOF) near Washington DC and into the Cloud. The CrIS SDR algorithm transforms the RDR into radiometrically and spectrally calibrated SDR product. RDR includes an engineering packet (EP) containing the calibration coefficients and science telemetry packets that carry dynamic calibration data. In this fashion, the calibration coefficients are made available to the users within the RDR data stream.

IDPS had generated two distinct CrIS SDR products that are the nominal spectral resolution (NSR) and the full spectral resolution (FSR). The NSR product was discontinued on 2 November 2020. Table 1 shows the measurement characteristics of both resolutions. The NEdN will change depending upon the spectral resolution used. In this study, the pre-launch NEdN calculations were made using NSR resolution because the instrument sell-off requirements are defined at this resolution only. Moreover, an off-line utility calculates the NEdN time series using the Allan deviation [6] at NSR because it is a legacy application from the S-NPP mission. The post-launch NEdN calculations were made using FSR resolution because the FSR radiance product is used for the retrieval of certain trace gases such as CO. The FSR NEdN plots show the expected higher noise levels present with finer spectral resolution combined with more noise due to a higher degree of interferometer self-apodization correction.

Table 1 CrIS Measurements Characteristics

Band	Spectral Range (cm^{-1})	NSR Spectral Resolution (cm^{-1})	FSR Spectral Resolution (cm^{-1})	NSR number of spectral channels	FSR number of spectral channels
LWIR	650 - 1095	0.625	0.625	713	713
MWIR	1210 - 1750	1.25	0.625	433	865
SWIR	2155 – 2550	2.5	0.625	159	633

The CrIS SDR operational algorithm calculates the NEdN expressed in spectral radiance units of $mW/m^2/sr/cm^{-1}$. The NEdN calculations use the ICT and deep space calibration measurements [7].

Both pre-launch and post-launch operational algorithms generate the NEdN estimates based on the calibration views at the given user's frequency grid (as opposed to the laser or sensor frequency grid). This work presents the NEdN estimated with four methods that are: 1) Operational algorithm based on the ICT and DS calibration views, 2) Off-line algorithm based on the singular value decomposition or Principal Component Analysis (PCA) using only post-launch Earth scene views where the spectra are arranged in a rectangular matrix, 3) Offline PCA algorithm using Earth views only where the spectra are modified into a squared matrix, and 4) Modified operational algorithm incorporating the Allan deviation. Section II has a discussion on the noise contributors. Section III presents the NEdN estimate methodologies. Section IV presents the pre-launch NEdN. Section V presents the post-launch NEdN. The results in section V show the instrument noise full correlation matrix, the noise history since the beginning of the mission, the noise dependency on the Earth scene brightness temperature (BT) and the geographical regions, and the noise prediction into 2025.

II. Noise Contributors

The total noise of the CrIS instrument has the contribution of several of its systems and subsystems. Zavyalov [8] has a list of several noise contributors. They are: 1) Shot noise (has dependency on the instrument background and the scene photon flux), 2) Metrology signal-to-noise-ratio (SNR), 3) Optical path difference (OPD) velocity noise [9], 4) FTS tilt noise [10], 5) Quantization noise introduced by the analog to digital converter (AD/C), 6) Detector 1/f noise [11], 7) Electronics noise, and 8) Johnson noise (electronics thermal dependency) [12]. The dominant noise sources for CrIS in the LWIR and MWIR bands are photon shot noise and AD/C quantization noise.

.

The photons absorbed by the detector create an electrical current. The corresponding current induced shot noise follows the Schottky formula [13] and is expressed as

$$i_{noise} = \sqrt{2\,I\,q} \tag{1}$$

where i_{noise} is the electrical current noise density at the detector in $Amp/\sqrt{Hz}$, I is the detector dark plus photon induced current in Amps, and q is the electron charge in Coulomb. In a straightforward way, the electrical noise at detector is transformed into an equivalent radiance noise at instrument input when this detector noise is divided by the instrument responsivity function [14]. The NEdN is expressed as

$$NEdN_i = \frac{i_{noise}}{A\Omega\,.\tau_o\,.\,\rho\,.\,\Delta\upsilon} \tag{2}$$

where the $NEdN_i$ is the noise of the induced electrical current and has the unit in W/m^2/sr/cm^{-1} , $A\Omega$ is the etendue (throughput) of the instrument defined by the steradian view of the instrument aperture area (sr-m^2), τ_o is the optical attenuation of the instrument, ρ is the detector responsivity (A/watt), and $\Delta\upsilon$ is the FTS spectral resolution (cm^{-1}). Detailed formulation of the other noise contributors would be cumbersome and complex, hence they are not presented in this work.

The instrument builder L3Harris developed the models for the various noise contributor types as presented in Zavyalov [8]. Compared to the S-NPP CrIS, the NOAA-20 CrIS has higher quantization noise primarily due to higher instrument throughput and lower electrical amplifier gain in the MWIR band by about 20%. Other additional noise features can be present in photovoltaic HgCdTe IR detectors. This is because HgCdTe detector material does not produce as good of a defect free structure as silicon detectors. The defects can change character over time and migrate when thermally cycled over large temperature ranges. This can results in changes of detector noise characteristics. Moreover, such a detector can have higher non-linearity signature. For instance, the MWIR FOV7 detector on the CrIS S-NPP satellite has higher noise and higher non-linearity compared with the other MWIR detectors [8, 15, 16]. Non-linearity estimates for NOAA-20 detectors are found in [17].

External mechanical vibration of the FTS instrument can introduce additional noise by modulating optical alignments. At the time of this writing, the NOAA-20 CrIS has not experienced discernable externally induced vibration noise.

Another noise feature is related to the CrIS SDR ground data processing. The truncation of the interferogram from FSR to NSR results in a noise reduction in two ways. First, the NEdN decreases for NSR because of a larger spectral resolution compared to the FSR mode of operation. Secondly, NEdN decreases further when operated in NSR mode because the interferometer self-apodization loses are reduced for shorter OPD length interferograms especially for the CrIS off-axis FOVs in the SWIR band. The effect is expressed as

$$NEdN_{FSR} = NEdN_{NSR}\left(\sqrt{\frac{NP_{FSR}}{NP_{NSR}}}\right)G_{ILS} \tag{3}$$

where NP_{FSR} and NP_{NSR} are the number of data points of the interferogram for FSR and NSR respectively. The term G_{ILS} represents the noise contribution due to self-apodization correction effect as described by Han et al. [18]. In this work, the noise specifications presented in the plots do not include the G_{ILS} term. Otherwise, a single noise plot will need to be replaced by three plots representing the center, side, and corner FOVs separately.

III. Noise Calculation Methodologies

A. Operational NEdN (Method 1)

The calculation of the CrIS NEdN is routinely performed by the operational SDR algorithm by using the calibration views of the ICT and DS occurring every 8 seconds. A moving window of these measurements spanning 4 minutes (ensemble of 30 calibrated ICT spectra) is used to estimate a calibrated mean and standard deviation for purposes of NEdN calculation [7]. The choice of 30 scans in the moving window was implemented by the ground data processing of the S-NPP CrIS as a mean to reduce the noise as much as possible for the benefit of the numerical weather prediction. In the interest of continuity and consistency, the NOAA-20 CrIS ground data processing also kept the moving window size to 30 scans. As part of a sensitivity study, a simulation shows that a reduction of the moving window size leads to an increase of the noise as shown in Figure 1. In this latter figure, the noise increase is expressed as percentage with respect to the window size of 30 scans. It is worth noticing that a window size of 12 scans increases the noise by about 3 %.

The ICT radiance spectra $L^*_{ict,i}$ are individually calculated for each of the nominal 30 scans calculated as

$$L^*_{ict,i} = \frac{(S_{ict,i}-\langle S_{ds}\rangle)}{(\langle S_{ict}\rangle-\langle S_{ds}\rangle)}L_{ict,i} + \frac{(\langle S_{ict}\rangle - S_{ict,i})}{(\langle S_{ict}\rangle-\langle S_{ds}\rangle)}L_{cold,i} \tag{4}$$

where $S_{ict,i}$ is an individual ICT raw spectrum corrected for non-linearity, within the sliding window for index *i* (0 to 29). The terms $\langle S_{ict}\rangle$ and $\langle S_{ds}\rangle$ are the average raw spectra over the sliding window of the ICT and DS respectively. The term $L_{ict,i}$ is the ICT black body cavity modeled radiance for the sliding window at index *i* and represents the hot radiometric reference. The term $L_{cold,i}$ is the deep space radiance that is set to zero on-orbit, and represents the cold radiometric reference. All the terms in Eq. 4 are separated by frequency bands, the FOV (FOV 1 to FOV 9), and the mirror sweep direction. During the TVAC testing, the term $L_{cold,i}$ refers to the radiance of the space calibration target (SCT) that is maintained at very cold temperature of about 100K and is defined as

$$L_{cold,i} = \epsilon_{cold,i}\beta(\sigma_i, T_{cold,i}) \tag{5}$$

where $\epsilon_{cold,i}$ is the effective emissivity of the cold SCT and the Planck function $\beta(\sigma, T_{cold,i})$ term is evaluated at the sensor (or laser) frequency grid σ at the temperature $T_{cold,i}$ for the ith sliding channel index.

The term $L_{ict,i}$ is defined as

$$L_{ict,i} = \epsilon_{ict,i}\beta(\sigma_i, T_{ict,i}) + (1-\epsilon_{ict,i})R_{refl,i} \tag{6}$$

where $\epsilon_{ict,i}$ is the ICT effective emissivity, $\beta(\sigma, T_{ict,i})$ is the Planck function at the sensor frequency grid σ_i and the temperature $T_{ict,i}$ in Kelvin. The term $R_{refl,i}$ refers to the ICT environmental model component that accounts for radiance outside the ICT that is reflected by the ICT back toward the detectors as described in the CrIS ATBD document [7].

From Eq. 4, a nominal ensemble of 30 ICT radiance spectra are collected. The operational NEdN estimates from this ensemble is given by

$$NEdN_{oper} = SMOOTH\Big(REAL\Big(STDEV\big(CMO * L^{*}_{ict,i}\big)\Big)\Big) \quad (7)$$

where the Correction Matrix Operator (CMO) is a square matrix that accounts for the post-calibration filter (or guard band) designed to suppress the out-of-band signal, the self-apodization correction, and the resampling from sensor frequency grid to the user frequency grid. The STDEV() operator calculates the standard deviation at each of the frequency bins, the REAL() operator retains only the real part of the complex spectra, and the SMOOTH() operator is a 17 points moving average across the frequencies. The NEdN reported in the CrIS SDR product shows the values on the user grid within the in-band user frequency range.

B. PCA NEdN Using Rectangular Matrix (Method 2)

An alternative NEdN calculation methodology uses the Principal Component Analysis (PCA) also known as the Singular Value Decomposition [19, 20, 21]. The computational steps are described in details by Turner et al. [19]. An ensemble of *m* spectra each containing *n* spectral frequency forms the *m* by *n* collection matrix A (m > n). For every frequency of the collection matrix, its mean is removed and scaled (divided) by the known operational NEdN from Eq. 7. The next step is to perform the singular value decomposition of the matrix *A* such that

$$A = USV^{T} \quad (8)$$

where *A* is *m* x *n* matrix , *U* is *m* x *m* orthogonal matrix , S is *m* x *n* diagonal matrix, *V* is a *n* x *n* orthogonal matrix. The matrix *S* has the eigenvalues in decreasing order on its diagonal. The next step is to transform the *S* matrix by retaining only the k (integer) highest eigenvalues and set the other eigenvalues to zero. This gives the S^{*} matrix. The backward calculation gives the reconstruction signal stored here in the A^{*}_{recon} matrix that has the same dimensions as the original *A* matrix. From the difference between the *A* and the A^{*}_{recon} matrices, the covariance and correlation matrices are calculated in a straightforward way. The key to this methodology is the selection of the integer k. For an integer k too small, the reconstructed matrix will have a deficiency of the radiance signal. An integer k too high will reduce the noise estimates that may not reflect the actual instrumental noise. To address this matter, Malinowski [22, 23, 24] introduced the factor indicator function (IND). This IND criteria minimizes the second norm of the reconstruction error matrix in relation with the number of spectra, the number of frequencies and the calculated eigenvalues. The minimum of the IND curve gives the k integer. The IND implementation assumes a signal random Gaussian noise that is constant in time and for every signal bins. The CrIS spectra does not meet one of the two assumptions as the noise is not constant at every frequencies. Attempt to determine k with IND on CrIS data did not give satisfactory results. A careful examination of the principal component matrices lead to the following guidelines for the selection of the k integer. They are:

1) The curve of the eigenvalues given by the S matrix becomes asymptotic. The selected k integer must be part of the asymptotic lower part of this curve.

2) The noise estimated by the PCA method should have the same shape and have values that appears similar to the operational noise. The use of a k integer that is too small has the effect of creating a noise estimates that resembles the radiance signal instead of looking like the operational noise.

3) An individual row of the V^{T} matrix contains the spectral signal affiliated with a given eigenvalue. A row associated with a high eigenvalue has strong spectral signal. A row with small eigenvalue shows white noise like characteristics. As guideline, the chosen k integer would correspond to the smallest eigenvalue where the row shows spectral signature.

We now introduce the relative reconstruction score R_{score} which is defined as

$$R_{score} = \frac{\|A^{*}_{recon}\|^{2}}{\|A\|^{2}} \quad (9)$$

where the second norm of a matrix corresponds to

$$\|A\|^{2} = \left(\sum_{i=1}^{m}\sum_{j=1}^{n}\left|a_{i,j}\right|^{2}\right)^{1/2}. \quad (10)$$

In this manuscript, the R_{score} quantity is used to determine the values of k. Additional work would be needed to determine whether or not this quantity can be used as criteria for selection the k integer.

C. PCA NEdN Using Square Matrix (Method 3)

The third methodology also is based on the PCA method. The A matrix from Eq. 8 is transformed into a squared matrix A_sq described by Serio [25] where Asq is defined as

$$A_{sq} = \frac{1}{m}(A^{T}A) \quad (11)$$

The A_{sq} matrix has a dimension of 2211 by 2211 that is subject the PCA decomposition generating the U, S, and V matrices as in Eq. 8. The term m is the number of observed radiance spectra. After removing the highest eigenvalues, the covariance and correlation matrices are calculated from the reconstructed

squared A matrix as described in [25]. The selection of the k parameter (eigenvalue cutoff point) was investigated using three techniques. The first technique is the use of the aforementioned IND criteria. The second technique is the Bayesian information criteria or BIC [26, 27, 28]. The third technique is the Akaike information criteria or AIC [29, 30].

D. Allan NEdN (Method 4)

The fourth methodology refers to the Allan deviation [31, 32]. Essentially, an observation is removed from the next observation, hence removing temporal noise processes. Applied to the CrIS observations, the Allan NEdN is defined as [33]

$$NEdN_{Allan}^{ict} = Real\left\{\left(\frac{1}{2m^2(N-2p+1)}\sum_{j=1}^{N-2p+1}\left(\sum_{i=j}^{j+p-1}(\Delta L)^2\right)\right)^{1/2}\right\} \quad (12)$$

and

$$\Delta L = \left(L_{ict,i+p}^{*} - L_{ict,i}^{*}\right) \quad (13)$$

where N is the total number of observations (e.g. 30 for a sliding window), p refers to the number of overlapping observations, and $L_{ict,i}^{*}$ is the ICT spectral radiance of Eq. 4. For instance, the temporal noise process can be caused by a time variation of the instrument radiance offset (or radiance self-emission term) which has a noticeable once per orbit signal.

IV. Pre-launch Results

Pre-launch tests have the goal of characterizing the CrIS instrument as well as ensuring that the requirements are met. The instrument was subjected to various testing environments. They included: 1) Bench testing (room environment), 2) Dynamic interaction or vibration, 3) Electromagnetic interference (EMI), and 4) Thermal vacuum (or TVAC).

During the dynamic interaction testing, the instrument was subjected to various external induced mechanical vibrations. Figure 3 shows the NEdN estimates for induced vibration along the X-axis at 95.6 Hz with an amplitude of 6 mG. The vibration signature is most significant for the SWIR at the beginning of the band from 2150 cm^{-1} to 2150 cm^{-1}. Moreover, the vibration induced NEdN degradation shows a FOV spread in the SWIR band.

During the TVAC testing, the estimation of the noise was performed for various settings. These settings vary the instrument voltage, temperatures of the external calibration target (an external hot black body cavity), and instrumental temperature plateaus. There are three temperature plateaus: 1) the mission nominal (MN), the Proto Flight Low (PFL), and Proto Flight High (PFH) where the CrIS instrument temperatures were set to about 278K, 260K and 310K respectively. The rationale for testing at these temperature plateaus is to ensure that the instrument can operate on-orbit for a wide range of temperature conditions. For the CrIS on S-NPP, there were 4 TVAC sessions (TVAC1 to TVAC 4). During TVAC4, there were three full cycles of temperature plateaus (MN, PFL, PFH). For CrIS on NOAA-20, there was one TVAC session during which there were eight full temperature cycles. At each of these plateaus, the NEdN collections consisted of acquiring in the staring mode the measurements of the ECT at 287K, the cold black body and the ICT.

Figure 3 shows the NEdN estimates at MN with the ECT at 287K during plateau number 7 with the ICT temperature set to 286.1K. In a similar way, the NEdN was estimated for the PFL and PFH plateaus where the ICT temperatures were set to 262.4K and 314.6K respectively. The CrIS instrument performs well within the temperature range from 262K to 314K. For both S-NPP and NOAA-20, the PFL noise has lower values than MN, and the PFH noise has higher values than MN. The background shot noise offers an explanation as the increase of photon flux increases the noise, since this noise source represents the major noise contributor over the SWIR band and dominates over the quantization noise. Two small artifacts were found related to the PFL and PFH noise. The MN FOV noise have a slightly tighter grouping than that of PFL and PFH (not shown). The root cause is not known but a possible explanation is the temporal temperature variation of the ECT that affected some FOV more than others. This grouping effect is found not to be significant. The second artifact is that the PFH noise within the SWIR frequency range from 2150 to 2200 cm^{-1} has a sharper noise increase compared to the remaining portion of the band. The root cause is not formerly known but a possible root cause is the vibrational induced noise by the TVAC environmental testing equipment.

V. Post-Launch Results

A. Operational Noise Estimates

After three months of outgassing, the NOAA-20 CrIS instrument became operational following the early on-orbit check out phase. This latter phase included powering up the instrument, optimizing the electrical gains and many other functioning parameters. The first light data became available on 5 January 2018. The IDPS ground processing segment generated the first CrIS radiance product using the calibration coefficients derived during the TVAC activities (EP version 112). Figure 4 presents the operational NEdN (method 1). The first light on-orbit NEdN gave two important takeaways.

The first major takeaway is that the MWIR FOV9 detector channels has higher noise and is out-of-family with respect to the other detectors of the MWIR band which is consistent with the TVAC measurements. The MWIR FOV9 detector has also higher non-linearity characteristics [17] where the so-called "a2" non-linearity quadratic coefficient correction has a significant value of 0.081 (from engineering packet version 115) whereas the other eight MWIR detectors have "a2" values

near zero. Here, the "a2" coefficients are used by the CrIS SDR algorithm for non-linearity correction [7]. For comparison purposes, the CrIS S-NPP MWIR FOV7 detector also had high noise and a non-linearity quadratic coefficient value of 0.107 which is also out-of-family. The first light on-orbit data showed that the noise of MWIR FOV9 remained about the same as during the pre-launch TVAC testing. The relation between the high non-linearity and the high noise is not well understood. Possible explanations include : 1) Lattice defect of the HgCdTe material as previously mentioned in section II, 2) HgCdTe contamination with impurities, 3) Issue with the contact between the HgCdTe material and the read-out integrated circuit (ROIC), and 4) Electronic noise inducted by the ROIC and/or the pre-amplifier. Pre-flight testing of the analog-digital converter (AD/C) strongly suggests that this component is not the root cause.

The second takeaway is that no external mechanical vibration induced noise was detected. The TVAC noise in Figure 2 shows higher noise in the 2150 to 2300 cm^{-1} spectral range as well as a greater noise spread across the FOVs that is characteristic of such aforementioned induced noise. Figure 4 does not show such higher noise and FOV spread which indicates that the on-orbit external mechanical induced noise effects, if any, have very small impact on the instrument noise. External mechanical vibration may add jitter to the various mirrors of the CrIS instrument, which in turn introduces noise into the interferogram. This result lead to the decision not to deploy the CrIS vibration isolation system on orbit. Since the beginning of the NOAA-20 mission, no evidence of significant noise increase related to external vibration has been observed.

B. Noise Estimates Using the PCA Methodology

The PCA methodologies allows evaluation of instrument noise performance over a wide range of Earth scene temperatures simply by processing a large ensemble of Earth scenes. Three sets of Earth scene data were examined using the PCA NEdN methodologies. The data set 1 collection occurred during the first 10 minutes past midnight on 20 August 2018. The ascending swath location is in the Pacific Ocean where the nadir FOR (FOR 15) latitudes went from -33.4 to -0.16 degrees and the west longitude went from -153.5 to -161.6 degrees. The Earth observations form a mixed combination of clear and cloudy scenes. The data set has 20 granules amounting to a total of 2400 spectra for each FOV. The Earth scene ensemble matrix subjected to the PCA method 2 has a dimension of 2400 by 2211 which forms the A matrix of Eq. 8.

In Figure 5, the subplots 5a, 5b, and 5c compare the operational NEdN (method 1) and the PCA NEdN using method 2 of data set 1 on a detector (FOV) basis. Figure 5d compares the operational NEdN (method 1) with the PCA method 3 for LWIR band only. Both PCA methods have very good agreement. In general, the NEdN derived from PCA are slightly lower than that of the operational NEdN. This was expected because the removal of the highest singular values might have removed some of the random noise signal. Examination of Figure 5 reveals that methods 1, 2, and 3 have good agreement. There are two significant exceptions. The PCA NEdN from method 2 has 30% higher values than that of of the operational NEdN (method 1) for LWIR FOV5. Even if the number of eigenvalues k be 121, instead of 61, for the signal reconstruction, the PCA NEdN would still have been 20 to 28% higher than that of the operational NEdN instead of 30%. The LWIR FOV5 has the strongest radiance signal of all detectors and its electrical gain setting is the lowest. After some investigation, it was discovered that patterns associated with the analog to digital converter (AD/C) quantization for FOV5 had been responsible for the noise difference. Figure 6 shows the diagnostic mode (DM) interferogram AD/C output count normalized distribution (interferogram integer values) that included more than 1080 interferograms for LWIR FOV 2 and LWIR FOV5 where the data were acquired on 19 January 2018. A DM interferogram has 21278 data point samples in the LWIR band. The AD/C digital output count distribution of FOV5 has the see-saw pattern in the top panel whereas the FOV 2 has a lot less of the see-saw pattern. The AD/C pattern noise is the result of the AD/C differential code nonlinearity where certain AD/C output codes are underrepresented and others are overrepresented. Because LWIR FOV5 has the lowest electrical gain among the LWIR FOVs, the AD/C pattern noise becomes more dominant under such conditions. This result illustrates the unique value provided by the PCA analysis method of computing the instrument NEdN which calculates the system NEdN using an ensemble of various Earth scenes, where each scene exercises the AD/C differently. AD/C pattern noise does not manifest itself when computing noise using the same scene repeatedly, as it is the case during ICT or deep space views.

Other factors could also contribute to observed noise differences. However, quantization noise has been identified as the major contributor. Both the operational and PCA LWIR FOV5 noise estimates met the specifications.

The second exception is the MWIR FOV9 where the PCA NEdN from method 2 is lower than the operational NEdN. A possible reason is that the reconstructed signal from the 61 singular values has some correlated and/or uncorrelated noise that ends up being removed. The PCA NEdN from method 3 also has lower values for the MWIR FOV9 detector (not shown).

The second data set analyzed 7 ensembles each grouped by 2 degrees Kelvin binned by brightness temperatures (BT) evaluated at the frequency 931.25 cm^{-1} and include all of the CrIS 3 bands. The seven BTs are 240.0K, 260.0K, 280.0K, 290.4K, 300.0K, 310.0K, and 320.0K. The Earth scene spectra have the individual LWIR, MWIR, and SWIR spectra for a total of 2211 channels. For instance, the 300K bin includes the Earth scene spectra when the BT is found to be between 299K and 301K. The integrated magnitude of the Planck function at the ICT on-orbit temperature of 278K corresponds closely to the integrated magnitude of the average Earth scene spectrum of the 290.4K BT bin ensemble. From the radiance ($Mw/m^2/sr$) point of view, this gives a basis for comparing the operational NEdN that is based on the ICT radiance and the NEdN derived from Earth scene views. A maximum of up to 3000

concatenated spectra are retained in each of the 7 ensembles. The PCA NEdN carried out the calculations for each separate FOV. Careful examination of the eigenvalue distribution for the various BT bins lead to the selection of 121 highest eigenvalues for the spectra reconstruction instead of the 61 for data set 1when using method 2. Specifically, the BT bins of 300K, 310K and 320K required additional eigenvalues for the reconstruction (Eq. 8) because the Earth scene signal is stronger. For the data set 1 and the case of data set 2 at 320K, the reconstruction scores of Eq. 9 and 10 are found to be 99.9982% and 99.9896 % respectively.

Figure 7 shows the change of the noise in percentage with respect to the mean noise accounting for all BT values for FOV 1 for both PCA method 2 and 3. In general, the NEdN is virtually unchanged for the cold BT bin and hotter BT bins for the LWIR and MWIR bands. However, the SWIR band shows a significant spread of the noise from the coldest to the hottest BT bin. This indicates the effect of the scene shot noise as a noticeable noise contribution factor due to its influence over the SWIR band. The PCA NEdN results for the other FOVs are similar to FOV1 and are not shown in here. Additional work revealed no difference of the calculated operational and PCA NEdN between the FTS mirror sweep directions. This was expected since the mirror sweep direction only impact the phase response of the output signal that is corrected by the radiometric calibration.

The third data set is a collection of seven sub data sets each representing a geographical region. Table 2 shows the geographical regions on 1 May 2020.

Table 2: Data set number 3 of seven geographical regions description on 1 August 2020.

Region	Min. Latitude	Max. Latitude	Min. Longitude	Max. Latitude	Comments
Tropical Land	-15.0	8.0	15.0	32.0	Africa
Tropical Ocean	-23.5	23.5	-180.0	-120.0	Pacific Ocean
Mid-Latitude Land	30.0	60.0	60.0	120.0	Asia
Mid-Latitude Ocean	-60.0	-30.0	-180.0	-120	Pacific Ocean
Desert	15.0	30.0	-10.0	30.0	Sahara
North Polar	70.0	90.0	-180.0	180.0	Arctic
South Polar	-90.0	-70.0	-180.0	180.0	Antartic

Figure 8 shows the noise change in percentage of the seven geographical region sub data sets for FOV 1 with respect to the mean of data set 3. Overall, the desert region has higher noise for all three bands. In the SWIR band, the polar colder region has lower noise and the desert area has the highest that is consistent with the effect of the scene shot noise contribution.

The magnitude of the noise change as function of the Earth scene temperature is small because two other noise sources dominate. The most important of these is the instrument background shot noise. The AD/C quantization noise also plays a dominant role in the LWIR and MWIR bands. PCA has essentially validated these predictions by observation of a wide range of calibrated Earth scene temperature spectra processed by CrIS.

The NEdN of these 3 data sets were recomputed using method 3. The selection of the eigenvalue cutoff point (k integer) using the BIC and AIC criteria gave poor results. In general, the BIC and AIC underestimated the k integer and the calculated NEdN showed spectra residual and the presence of numerous spikes corresponding to spectral lines. However, the use of the IND criterion gave good results. The comparison of the PCA NEdN between both methodologies 2 and 3 for data set 1 showed a difference of less than 5%. The MWIR FOV9 is the sole exception where the NEdN from method 3 is about less than 12% compare to method 2. The comparison of method 2 and 3 for data set 2 and 3, presented in Figures 7 and 8, shows that method 3 gives more consistent results between the BT bins and the geographical regions. In general, the PCA NEdN of method 2 and method 3 are within 10% of each another.

C. Full Correlation Factor Matrix

The PCA methodology also allows the calculation of the full spectral channel covariance matrix and correlation factor. Figure 9 shows the full correlation factor matrices computed with method 2 of FOV9 for LWIR, MWIR, and SWIR bands using data set 1 along with FOV5 for the LWIR band only. The corner FOV9 was selected because it has the highest ILS induced noise effect whereas FOV5 has the least. The 4 plots in Figure 9 exhibit four characteristics. They are:

1) Higher noise in the 650 to 800 cm^{-1} range due to a low instrument responsivity function (not shown) that produces a low signal to noise ratio (SNR). The low instrument responsivity in this range is caused by optical properties of the ZnSe beam splitter used in the FTS. However, the correlation factor in this range has small values and no significant correlation is found.
2) Strong correlated noise is indicated off the matrix diagonal mostly in the SWIR and diminishing in the MWIR. This is due to ILS self-apodization effect [18]. Self-apodization has a dependency on the FOV position and therefore distorts the ILS differently for each FOV. The distortion must be removed to obtain accurate and identical ILS for all instrument FOVs. The ILS correction is carried out by applying the inverse self-apodization (ISA) matrix multiplication as part of the calibration ground data processing. The ISA matrix contains higher values off the diagonal and thereby introduces a higher level of correlated noise in the result. Moreover, the generation of the operational NEdN product applies the ISA matrix multiplication and also results in having strong off-diagonal

correlation factor values. Figure 10 shows the correlation factor for the frequency 2531.125 cm^{-1} for cases: 1) FOV9 unapodized, 2) FOV9 with Hamming apodization, and 3) FOV5 unapodized. The unapodized FOV9 case shows the signature of the ILS effect where the correlation factor has a damped oscillation (up-and-down) pattern and declining away from the diagonal. This damped oscillation signature is not present for the unpodizated FOV5 for all three frequency bands which has no signicant ILS effect. The Hamming apodization case is presented as it is widely used in the downstream data processing for numerical weather prediction and atmospheric profile retrieval applications. It is worth noticing that the Hamming apodized correlation factor exists only for the two data points adjacent to the diagonal. The FOV5 unapodized case shows no off-diagonal correlation as this detector has no significant ILS effect.

3) Beside the ILS effect, careful examination of Figure 9 reveals that the 668.125 cm^{-1} frequency has strong off-axis correlation factor. Figure 11 presents the correlation factor R of the 668.125 cm^{-1} frequency with respect to the adjacent frequencies for both the unapodized and Hamming apodized cases. The spectral region from 650 to 700 cm^{-1} has a strong CO_2 atmospheric absorption where a typical Earth spectrum has a BT of about 220K. The noise at 668.125 cm^{-1} holds a high correlation against channels located around 690, 720.0, and 740 cm^{-1} frequencies. Some BTs exhibit anti-correlation features. The origin of the correlation about the 668.125 cm^{-1} frequency is not well understood at this time and is currently under investigation. The user should use caution when using this channel. Beside the 668.125 cm^{-1} frequency, the full correlation factor matrices of Figure 9 show no significant off-diagonal signal which is a testimony on how well the CrIS instrument is built.
4) Figure 9a also shows the presence of off-axis correlation factor for the LWIR FOV9 detector related to the CO_2 and O_3 atmospheric lines. The CO_2 atmospheric lines of interest are located in the 680 to 800 cm^{-1} spectral range that is used to retrieve the temperature profile. The O_3 atmospheric lines are located in the 1020 to 1070 cm^{-1} spectral range. For both of these two spectral ranges, the off-axis correlation factors have values within +/- 0.12. For the LWIR FOV5, the off-axis correlation factor is within +/= 0.05 for the same CO_2 and O_3 spectral ranges. This suggests that the ILS effect and its correction introduced small off-axis correlated noise in the LWIR band. These correlation factor values are not expected to be significant for the downstream products (Ken Pryor from NOAA, and James Jung from UW, personal communication). Moreover, examination of the correlation factor between the bands (LWIR-MWIR, LWIR-SWIR, and MWIR-SWIR) shows no off-axis correlation.

The PCA NEdN calculated with method 3 shows similar results as the PCA NEdN from method 2 regarding the correlation matrices (Figure 9), the correlation factor at 2531.25 cm^{-1} (Figure 10), and the correlation factor at 668.125 cm^{-1} (Figure 11).

Fundamentally, the operational NEdN calculation can provide only the information of the diagonal of the radiometric noise full covariance matrix and has no information about the correlation factor matrix. These two matrices can be obtained with the PCA methodology. These matrices off-diagonal terms have inter-channels correlation information that may be included as part of the downstream product estimation for weather forecast and atmospheric chemistry applications. For instance, strong inter-channel correlation might indicate issues with the instrument crosstalk that may give incorrect radiometric calculations.

D. Two Years of Noise History

The CrIS operational data processing generated the CrIS SDR first light data on 5 January 2018. The noise varied for several reasons over the course of two years of operation. Figure 12 presents the daily Allan noise (method 4) of the 1580 cm^{-1} frequency with the forward FTS sweep direction. The timeline is described below.

a) From 5 January to 17 January 2018, the data processing used the calibration coefficients derived during the pre-launch TVAC ground testing. This corresponds to the usage of the engineering packet (EP) version 112.
b) On 17 January 2018, refinement of the calibration coefficients were uploaded as part of the EP version 113. This lead to a decrease of the noise level.
c) On 2 February 2018, the CrIS instrument was placed in safe mode. After reset, incorrect bias tilt parameters were used. The bias tilt is the bias of the alignment between the porch swing mirror and the dynamic alignment system.
d) On 16 February 2018, the correct bias tilt parameters were uploaded leading to a decrease of the NEdN. The presence of the bias tilt reduces the amplitude of the modulated signal, hence increasing the noise. Simultaneously, further refinement of the calibration parameters were uploaded as part of the EP Version 114. The EP V114 upload lead to no significant improvement of the noise level. The EP V114 main contribution was to improve the geolocation accuracy.
e) On 16 July 2018, the instrument was placed on safe mode for a short period of time. After the reset, the incorrect bias tilt cause an increase of noise that lasted until 26 July 2018.
f) On 14 August 2018, several changes were made to the instrument parameters. The calibration parameters were further refined leading to the upload of the EP version 115. This latter version formed the basis for declaring the CrIS SDR as validated maturity level status. Moreover, the PGA received of boost of 50% affecting the MWIR FOV 1 to FOV 8 only. This led to a significant decrease of the noise for these 8 detectors

of about 15 to 20%. The MWIR FOV9 detector had already been optimized by setting a high PGA gain compared with the other detectors. It was recognized that no further noise reduction would be obtained by increasing the PGA gain even more. An increase of 3% of the downlinked data volume made this PGA boost possible. It took two orbits (about 3 hours 20 minutes) to perform the change. The EP version 115 is still operational at the time of writing.

g) On 3 December 2018, the instrument was place into safe mode with the loss of several orbit of data. During this time, the instrument warmed up. Upon reset, the various instrumental temperature cooled down for about 24 hours. During this 24 hours period, the NEdN was higher but came back to its level prior to the instrument reset.

In Figure 12, the MWIR FOV5 detector experienced a slow buildup noise increase in June 2019 until the date of 3 July 2019. Late on that day, the noise stepped down back to the previous nominal value. From July to December 2019, the same detector shows a gradual increase of the noise. The exact root cause is not determined at this time. However, the noise behavior affected only one detector. This suggests an electronic component, such as a capacitor, as being the root cause.

Figure 13 shows the Allan noise (method 4) at the 2515 cm^{-1} frequency since the beginning of the mission. For this frequency, the noise increases at an annual rate of about 1.36 e-4 R.U. per year.

E. Temporal Noise Change

The instrument responsivity function *R* (or gain) shows a decline since the beginning of the mission. In relation to the complex *R*, the raw complex spectra *S* can be expressed as

$$S_{ds} = R(\,O_{ds})$$
$$S_{ict} = R(\,L_{ict} + O_{ict}) \quad (14)$$

where *O* is the instrument self-emission term (complex), and the *L* terms are the actual real radiances of the deep space (DS) or ICT scenes. Because the ICT and deep space measurement were made very close in time, one can assume that the self-emission terms O_{ds} and O_{ict} are equal. From Equation 14, *R* and *O* are found to be

$$R = \frac{(S_{ict} - S_{ds})}{L_{ict}} \quad (15)$$

$$O_{ds} = \frac{S_{ds}}{R} \quad (16)$$

The instrument responsivity function R was calculated on 15 August 2018 and on 15 May 2019. Figure 14 shows the degradation of *R* in percentage on 15 May 2019 with respect to 15 August 2018 spanning a period of 9 months. The degradation of *R* has a strong 4% absorption feature at the MWIR frequencies at 1270 and 1720 cm^{-1} that may indicate the presence of chemical contamination. The SWIR also shows significant degradation of *R* of 2.5% or more in the 2400 to 2550 cm^{-1} spectral range. The degradation of *R* for CrIS NOAA-20 is about 4 times higher than that of S-NPP. Modeling *R(t)* as function of time as

$$R(t) = R_0 + \Delta R + \varepsilon \quad (17)$$

where R_0 is the responsivity function on 15 August 2018, ΔR is the linear rate of change of *R* based on Figure 14 and ε is the random noise term. Based on Equations 2 to 5, and 14 to 17, an algorithm was written that predicts the NOAA-20 NEdN in August 2025. The predicted noise is shown in Figure 15. After examination of the other FOVs, the NEdN is not expected to exceed the CrIS specification with the exception of MWIR FOV9. The noise difference at the frequency 2515 cm-1 adjusted on a yearly trend and transforming the FSR to NSR according to Eq. 3 gives a NEdN trend of 0.000121 Radiance Unit per year which matches closely the observed yearly trend of 0.000136 shown in Figure 13. With high confidence, we can state that the noise increase trend is due in good part to the degradation of the instrument responsivity function.

VI. Discussion and Conclusion

The NOAA-20 CrIS SDR radiance product meets the noise specifications with margin for all FOV detectors with the exception of the MWIR FOV9 which is borderline. Using the PCA methodologies, the full correlation matrix shows correlated noise at the frequency 668.125 cm-1 with stronger correlation with the 720.0 cm-1 frequency. Due to ILS algorithm correction, correlated noise near the diagonal is found affecting mostly the SWIR band and for the side and corner FOVs. This correlated noise is expected and is well understood. Noise estimates of the spectra binned by brightness temperature (BT) reveals that hot and cold Earth scenes have slightly different noise characteristics in the LWIR and MWIR bands. The noise increase is at least 20% between the coldest and hottest temperature bins for the highest frequency in the SWIR band. The LWIR FOV5 exhibits an out-of-family behavior. For this detector, the noise estimates using the PCA methodologies is significantly higher than that of the operational NEdN. The AD/C quantization pattern is believed to be the root cause.

The temporal change of the noise is due to several factors such as the instrument settings (bias tilt, PGA gain), the degradation of the responsivity function, and the instrument post reset state.

For the CrIS Earth scenes, the PCA method 2 did not gave good results when using either the IND, BIC or AIC criteria for the eigenvalues cutoff point. The PCA method 3 worked well for the IND criteria only and this method can be automated. However, this PCA method 3 does not allow the signal reconstruction, hence it cannot be used for denoising the Earth scene spectra. The next challenge is to find a cutoff point criteria that would work for the PCA method 2 for denoising purpose.

Overall, the NOAA-20 CrIS noise is very low. The global forecasting system (GFS) assimilates the CrIS radiance. Because the noise is very low, the GFS assimilation has errors that are dominated by the scene inhomogeneous state knowledge, the incorrect parameterization of the forward model and its smoothing effects, the presence of clouds, and the uncertainty of the surface characterization. However, the CrIS low noise allows to distinguish the radiometric bias between the FOVs (James Jung, UW, personal communication). Similarly, the atmospheric trace gas retrieval errors are dominated in the same fashion as the GFS assimilation errors (Ken Pryor, NOAA-STAR, personal communication). One aspect of the noise impact on the trace gas retrieval application is the channel selection. In the case where two channels are identified as candidates, the channel with the lowest noise would be selected.

ACKNOWLEDGMENT

This work was supported by the National Oceanic and Atmospheric Administration under contract ST133017CQ0050. The contents of this paper are solely the opinions of the authors and do not constitute a statement of policy, decision, or position on behalf of NOAA or the U.S. Government.

REFERENCES

[1] C. Rodgers, “Inverse methods for atmospheric sounding: Theory and Practice”, World Scientific Ed., Hackensack N.J., 2000

[2] A Gambacorta, C. Barnet, W. Wolf, T. King, E. Maddy, L. Strow, X. Xiong, N. Nalli, M. Goldberg, “An experiment using high spectral resolution CrIS measurements for atmospheric trace gases: Carbon monoxide retrieval impact study”, IEEE Geoscience and Remote Sensing Letters, Vol. 11, Issue 9, Sept. 2014.

[3] E. Dammers, M. Shephard, M. Palm, K. Cady-Pereira, S. Capps, E. Lutsch, K. Strong, J. Hannigan, I. Ortega, G. Toon, W. Stremme, M. Grutter, N. Jones, D. Smale, J. Slemons, K. Hrpcek, D. Tremblay, M Schaap, J. Notholt, and J. Erisman, “Validation of the CrIS fast physical NH3 retrieval with ground-based FTIR”, Journal of Atmospheric Measurement Techniques, 10, 2645-2667, 2017

[4] R. Eresmaa, J. Letertre-Danczak, C. Lupu, N. Bormann, and A. P. McNally, “The assimilation of Cross-track Infrared Sounder radiances at ECMWF,” Quarterly Journal of the Royal Meteorological Society, vol. 143, no. 709, pp. 3177-3188, 2017.

[5] C. Cao, Y. Chen, X. Jin, D. Tremblay, A. Wald, S. Kireev, H. Yu, L. Wang, “Cross Track Infrared Sounder (CrIS) Sensor Data Record (SDR) User’s Guide,” Version 1.1, April 2018. [Available online at https://www.star.nesdis.noaa.gov/jpss/documents/UserGuides/CrIS_SDR_Users_Guide1p1_20180405.pdf

[6] Y. Chen, F. Weng, Y. Han, “SI Traceable Algorithm for Characterizing Hyperspectral Infrared sounder CrIS Noise”, Applied Optics, Vol. 54, issue 26, pp. 7889-7894, doi:10.1364/AO.54.007889, 2015

[7] JPSS configuration management, ‘Joint polar satellite system (JPSS) Cross Track Infrared Sounder (CrIS) sensor data records (SDR) algorithm theoretical basis document (ATBD) for full spectral resolution, document number D0001-M01-S01-002_JPSS_ATBD_CrIS-SDR_fsr_20180614, 2018

[8] Zavyalov V., M. Esplin, D. Scott, B. Esplin, B. Bingham, E. Hoffman, C. Lietzke, J. Predina, R. Frain, L. Suwinski, Y. Han, C Major, B. Graham, and L. Phillips, “Noise performance of the CrIS Instrument”, Journal of Geophysical Research: Atmospheres, Vol. 118, 13,108-13,120, doi:10.1002/2013JD020457, 2013.

[9] Palchetti L. and Lastrucci D.:Spectral noise due to sampling errors in Fourier-transform spectroscopy, Applied Optics, Vol. 40, issue 19, pp. 3235-3243, doi:10.1364/AO.40.003235, 2001

[10] Wang X. and Cai X., "Analysis of mirror-tilting and sampling errors in Fourier transform spectrometry and design of error analysis Graphical User Interface," Proceedings of 2011 International Conference on Electronic & Mechanical Engineering and Information Technology, Harbin, 2011, pp. 3186-3189, doi: 10.1109/EMEIT.2011.6023051.

[11] Weissman, M. B.,’1/f Noise and other slow non-exponential kinetics in condensed matter”, Reviews of Modern Physics, 60,(2), 537-571, doi:10.1103/RevModPhys.60.537, 1988.

[12] Johnson J., “Thermal agitation of electricity in conductors: Physical Review, 32, (97), 350-373, doi:10.1103/physrev.32.97, 1928.

[13] Ott H., Noise reduction techniques in electronic systems, John Wiley, pp. 208, 218, 1976, ISBN 0-471-65726-3

[14] Schwantes K. R., D. Cohen, P. Mantica, and R. Glumb, “Modeling noise equivalent change in radiance (NEdN) for the Crosstrack Infrared Sounder (CrIS)”, Proc. SPIE 4489, Infrared Spaceborn Remote Sensing IX, (8 February 2002); https://doi.org/10.1117/12.455128

[15] D. Tobin, H. Revercomb, R. Knuteson, J. Taylor, F. Best, L. Borg, D. DeSlover, G. Martin, H. Buijs, M. Esplin, R. Glumb, Y. Han, D. Mooney, J. Predina, L. Strow, L Suwinski, and L. Wang, " Suomi-NPP radiometric calibration uncertainty", Journal of Geophysical Research: Atmosphere, Vol 118, 10,589-10,600, doi: 10.1002/jgrd.50809, 2013

[16] Y. Han, H. Revercomb, M. Cromp, D. Gu, D. Johnson, D. Mooney, D. Scott, L. Strow, G. Bingham, L. Borg, Y. Chen, D. DeSlover, M. Esplin, D. Hagan, X. Jin, R. Knuteson, H. Motteler, J. Predina, L. Suwinski, J. Taylor, D. Tobin, D. Tremblay, C. Wang, Lihong Wang, Likun Wang, V. Zavyalov, "Suomi NPP CrIS measurements, sensor data record algorithm, calibration and validation activities, and record data quality", Journal of Geophysical Research: Atmospheres, v 118, 12,734-12,748, do:10.1002/2013/2013JD020344, 2013

[17] NOAA configuration management, "Joint Polar Satellite System 1 (JPSS1) Cross Track Infrared Sounder (CrIS) Sensor Data Record (SDR) Calibration/Validation Plan",volume 1, 31 December 2015, available online at https://www.star.nesdis.noaa.gov/jpss/Docs.php

[18] Y. Han, L. Suwinski, D. Tobin, and Y. Chen, "Effect of self-apodization correction on Cross-Track Infrared Sounder radiance noise", Appl. Opt, Vol. 54, No 34, doi:10.1364/AO.54010114

[19] D. Turner, R. Knuteson, and H. Revercomb, "Noise reduction of atmospheric emitted radiance interferometer (AERI) observations using principal component analysis.", Journal of atmospheric and oceanic technology, Vol. 23, 1223,-1238, 2006

[20] V. Zavyalov, C. Fish, G. Bingham, M. Esplin, M. Greenman, D. Scott, and Y. Han, "Preflight assessment of the cross-track infrared sounder (CrIS) performance", Proc. SPIE, Vol. 8176, Sensors, Systems, and Next-Generation Satellites XV, 817606 (3 Oct 2011): doi: 10.1117/12.897674: https://doi.org/10.1117/12.897674

[21] D. Tremblay, Y. Han, Y. Chen, X. Jin, L. Wang, and Q. Liu, "CriS SDR Calibration and validation status and NOAA-STAR related activities.", Proc. of SPIE Vol85280, 85280F, doi: 10.1117/12.981340, 2012

[22] Malinowski, E. R, : Theory of error in factor analysis. Anal. Chem., Vol. 49, 606-612, 1977a

[23] Malinowski, E. R, : Determination of the number of factors and the experimental error in a data matrix, Anal. Chem., Vol. 49, 612-617, 1977b.

[24] Malinowski, E. R. : Factor Analysis in Chemistry, 3rd ed., Wiley and Sons, 414 pp., 2002.

[25] Serio C., Masiello G., Camy-Peret C., Jacquette E., Vandermarcq O., Bermudo F., Coppens D., Tobin D., "PCA determination of the radiometric noise of high spectral resolution infrared observations form spectral residuals: Application to IASI", Journal of Quantitative Spectroscopy and Radiative Transfer, 206, 2018, 8-21, https://doi.org/10.106/j.jqsrt.2017.10.022

[26] Schwarz G. "Estimating the dimension of a model", Ann. Stat., 6 (2), 461-464, 1978, doi: 10.1214/aos/1176344136

[27] Michael E.T. Christopher M. B., "Probabilistic principal component analysis", J. R. Stat. Soc. Ser. B, 1999, 61 (3), 611-622

[28] Minka T.P., "Automatic choice of dimensionality for PCA", Adv. Neural Inf. Process. Syst., 2000, 322 (5904), 577-583, doi:10.1126/science.1164015

[29] Akaike H., "A new look at the statistical model identification." IEEE Trans. Autom. Control, 1974, 19 (6), 716-723, doi: 10.1109/TAC.1974.11007705.

[30] Bedrick, E.J., Tsai C-L., "Model selection for multivariate regression in small samples", Biometrics, 1994, 50 (1), 226-231

[31] D. Allan, N. Ashby, and C.C. Hodge, "Appendix A: time and frequency measures accuracy, error, precision, predictability, stability, and uncertainty", in *The Science of Timekeeping*, Hewlett Packard Application No 1289, p. 59 (1997)

[32] IEEE Standards Coordinating Committee 27 on Time and Frequency, "IEEE standard definitions of physical quantities for fundamental frequency and time metrology random instabilities", IEEE Standard, 1139-1999, p. 31 (IEEE, 1999)

[33] Y. Chen, F. Weng, Y. Han, "SI traceable algorithm for characterizing hyperspectral infrared sounder CrIS noise", Applied Optics, Vol. 54, no. 26, September 2015, doi:10.1364/AO.54.007889

FIGURES

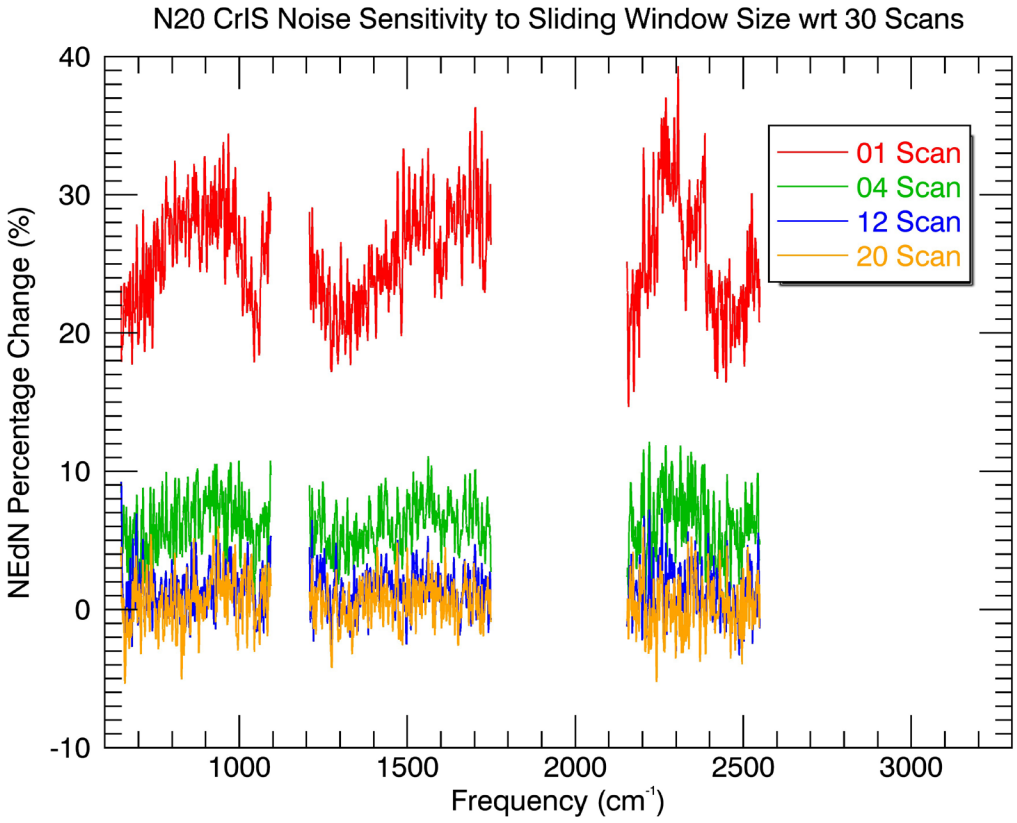

Figure1: Noise change sensitivity on the number of spectra (scans) in the sliding window with respect to the current window of 30 scans.

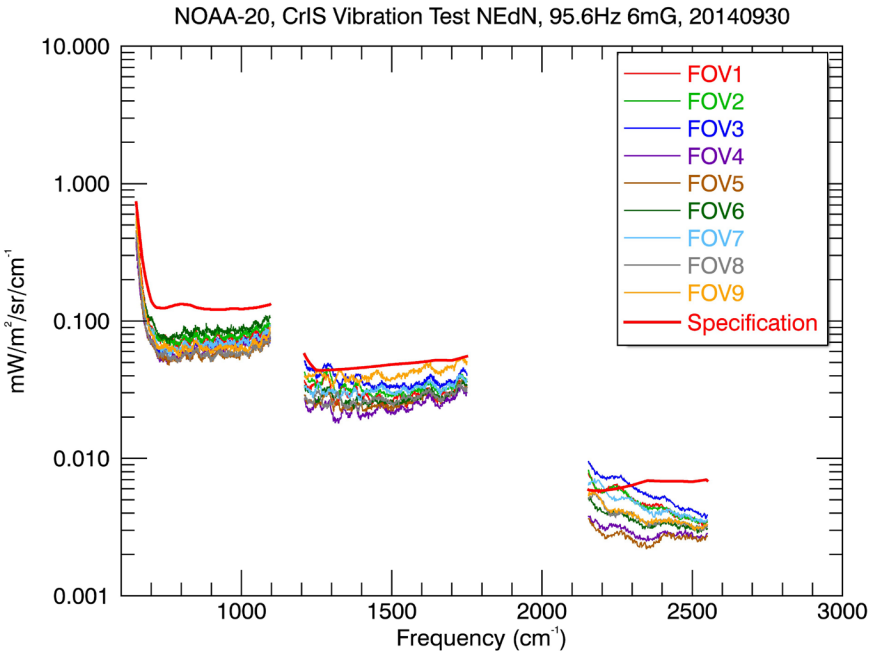

Figure 2: Noise estimates during the dynamic interaction test with vibration induced along the X-axis at 95.6 Hz and at 6 mG.

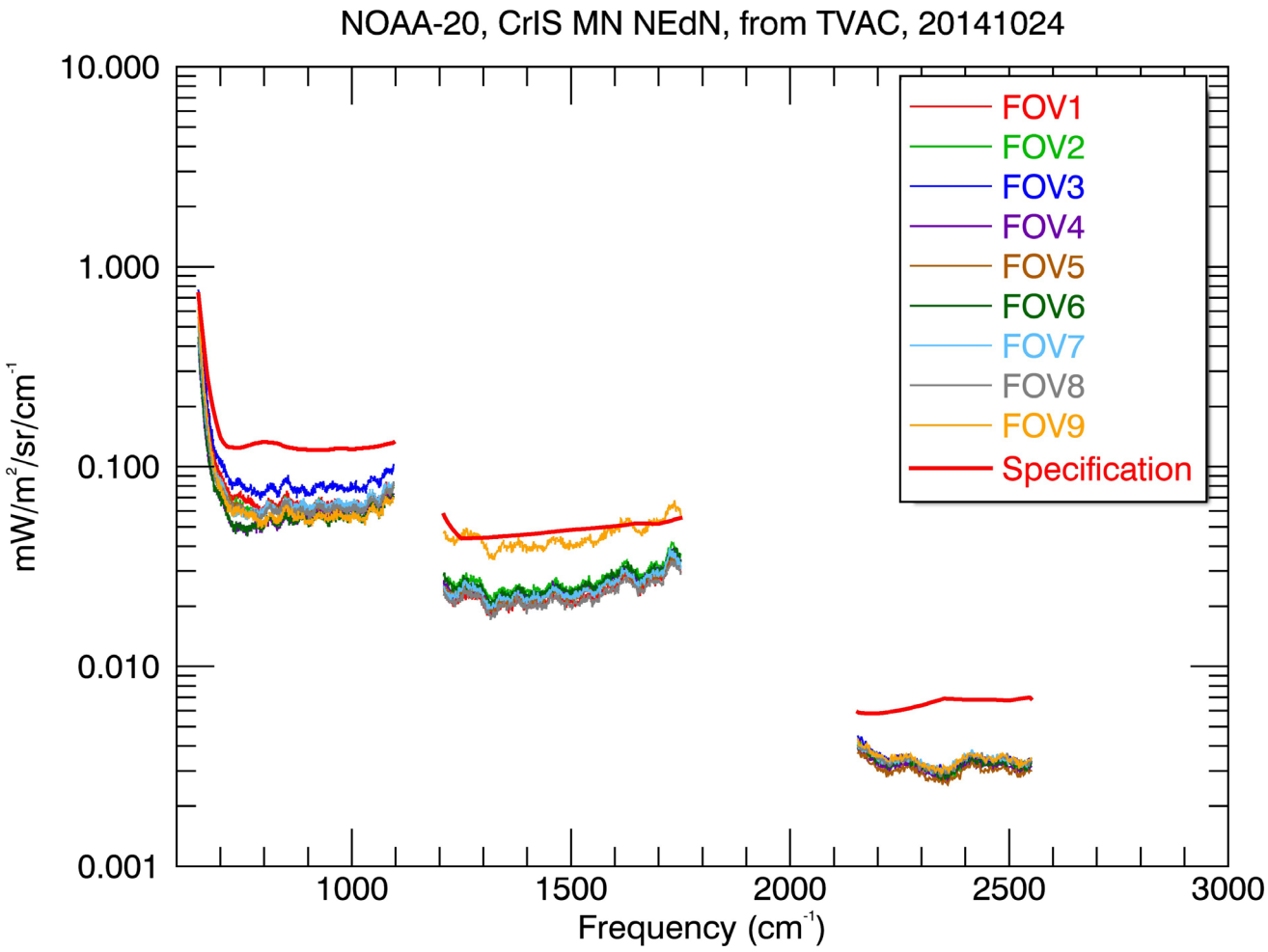

Figure 3: NSR noise estimates at mission nominal during TVAC plateau 18 with ECT at 287K and electronics side 1 set at 30 volts.

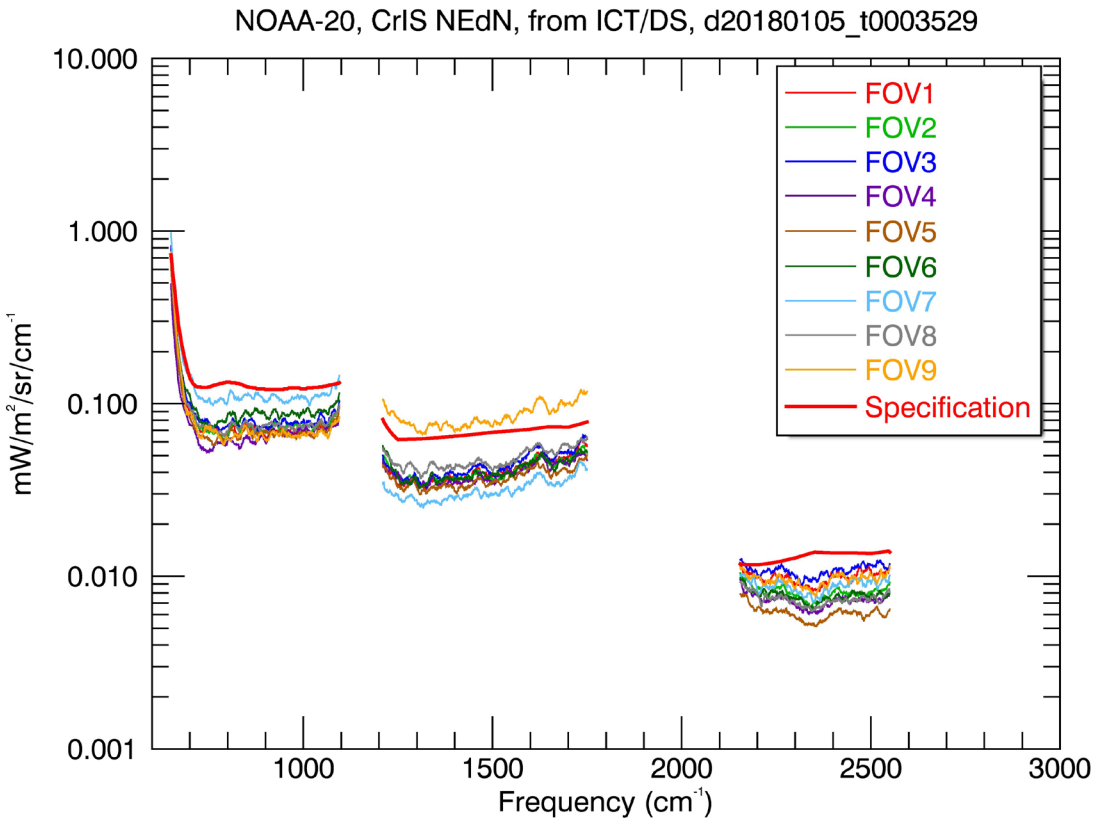

Figure 4: CrIS NOAA-20 first light operational NEdN on 5 January 2018.

a)

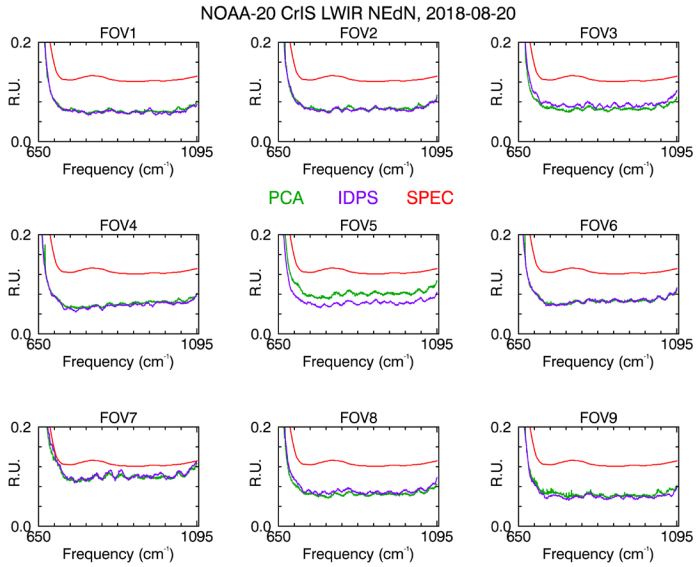
NOAA-20 CrIS LWIR NEdN, 2018-08-20
FOV1
FOV2
FOV3
FOV4
FOV5
FOV6
FOV7
FOV8
FOV9
R.U.
0.2
0.0
650
1095
Frequency (cm-1)
PCA
IDPS
SPEC

b)

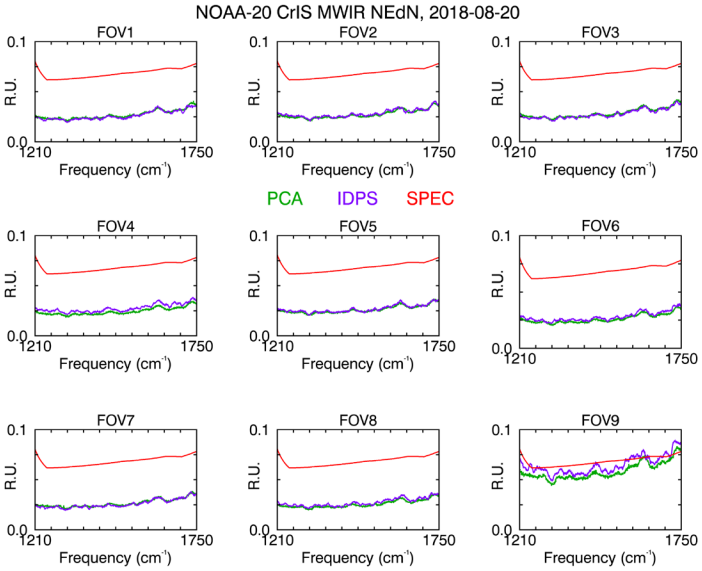
NOAA-20 CrIS MWIR NEdN, 2018-08-20
FOV1
FOV2
FOV3
FOV4
FOV5
FOV6
FOV7
FOV8
FOV9
R.U.
0.1
0.0
1210
1750
Frequency (cm-1)
PCA
IDPS
SPEC

c)

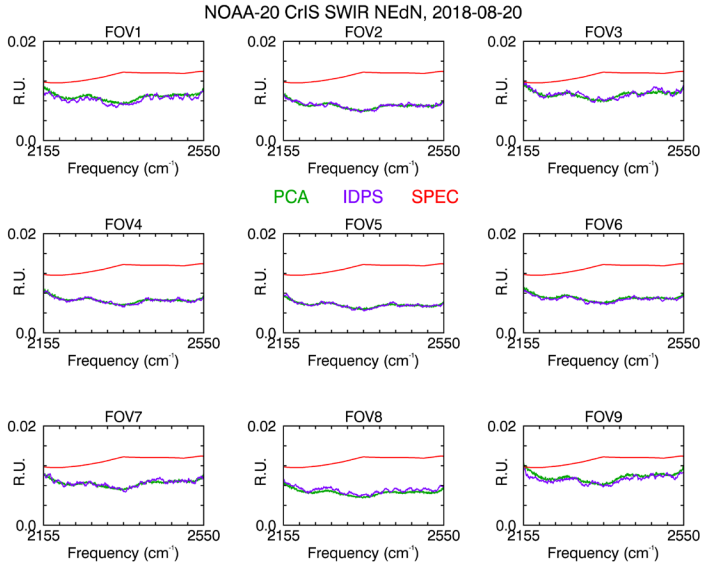

d)

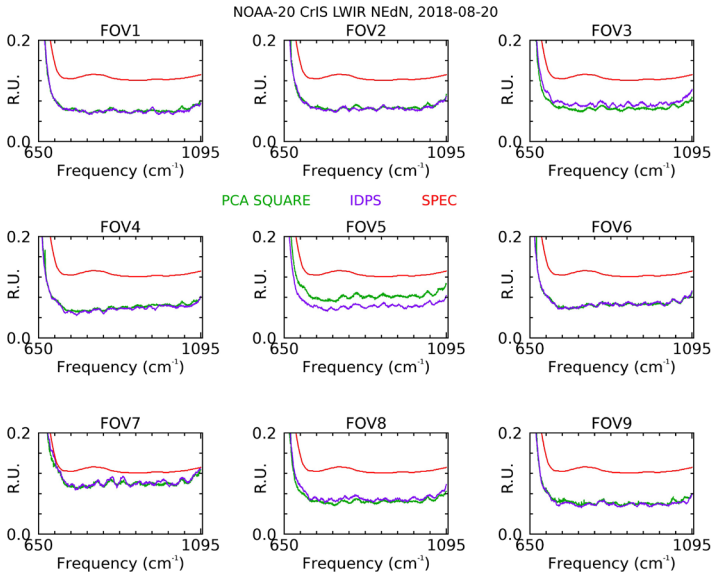

Figure 5: Operational IDPS (purple)) NEdN and data set 1 PCA NEdN using method 2 (green) comparison of the LWIR (a) , MWIR (b), and SWIR (c) bands, sweep direction 0. The NEdN calculated the PCA method 3 for the LWIR band (d).

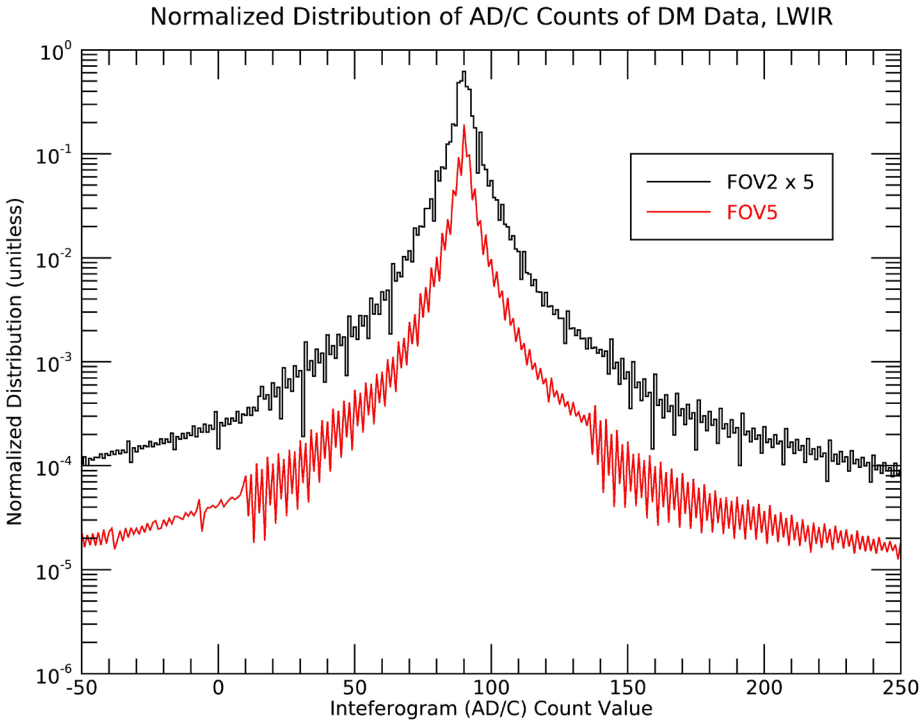

Figure 6: Normalized Earth scene (ES) interferogram AD/C count value distribution for FOV5 and FOV2 for sweep direction (SD) 0 using over 1080 diagnostic mode interferograms. The FOV 2 values were multiplied by 5 for presentation purpose.

a)

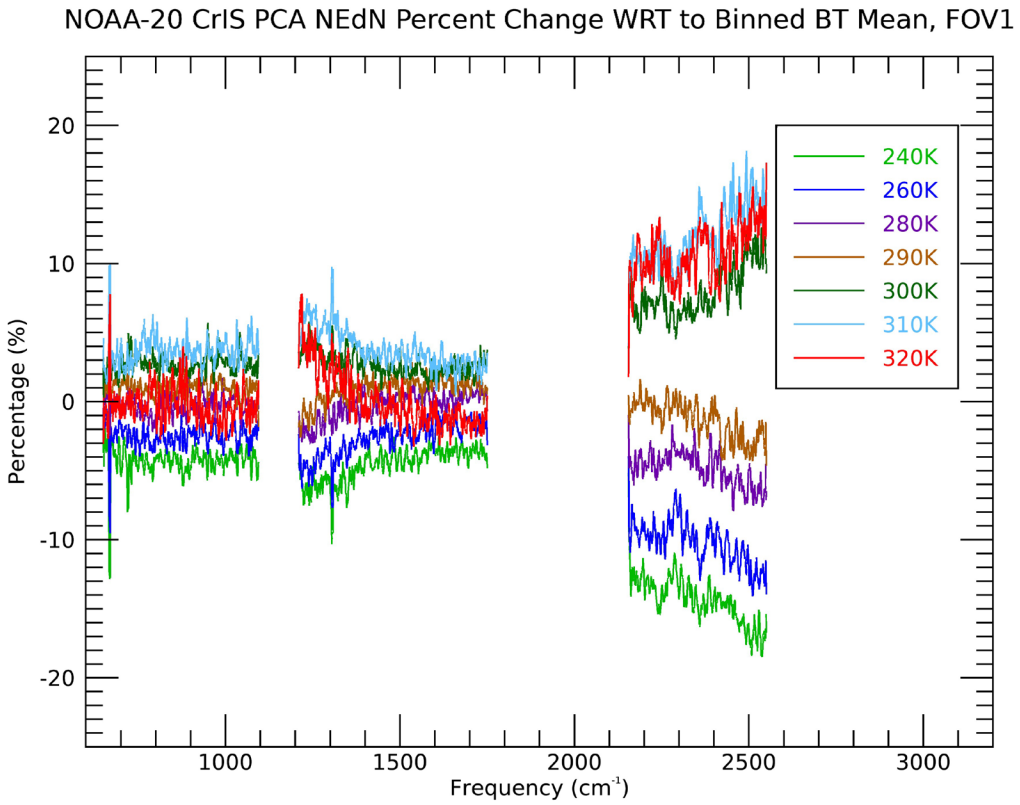
NOAA-20 CrIS PCA NEdN Percent Change WRT to Binned BT Mean, FOV1
Percentage (%)
20
10
0
-10
-20
1000
1500
2000
2500
3000
Frequency (cm-1)
240K
260K
280K
290K
300K
310K
320K

b)

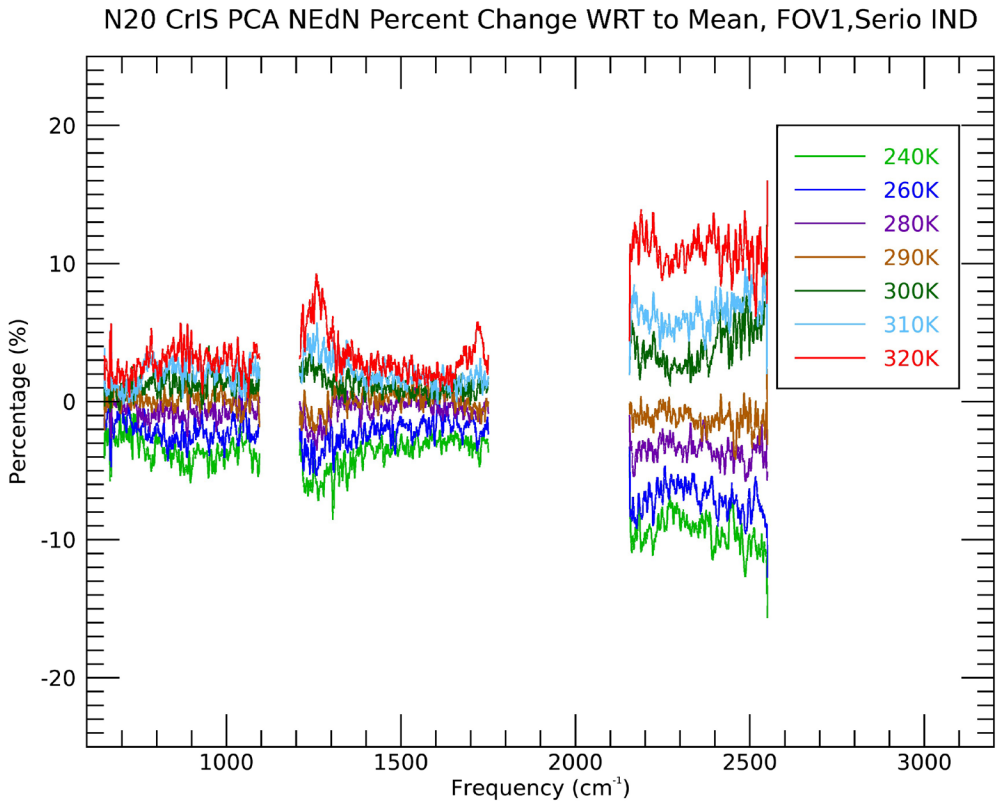

Figure 7: PCA noise change in percentage of the BT binned from data set 2 with respect to the overall mean noise for FOV1 using method 2 (a) and the method 3 with the IND criteria (b) .

a)

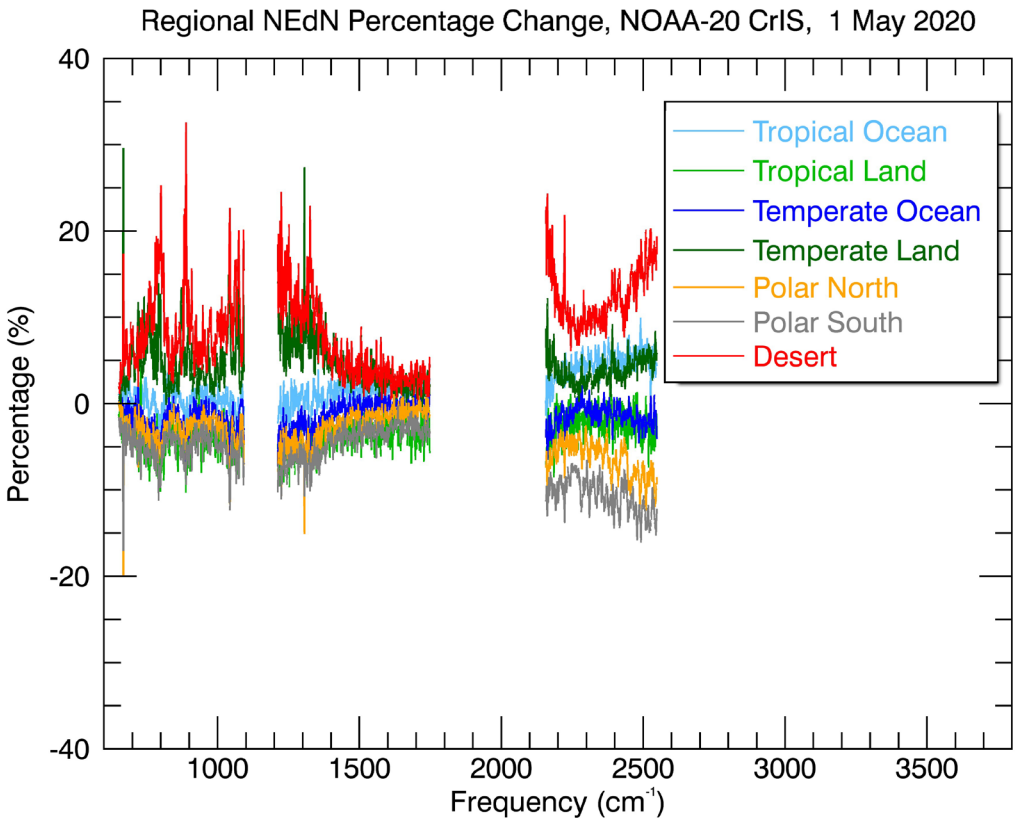
Regional NEdN Percentage Change, NOAA-20 CrIS, 1 May 2020
Percentage (%)
40
20
0
-20
-40
1000
1500
2000
2500
3000
3500
Frequency (cm-1)
Tropical Ocean
Tropical Land
Temperate Ocean
Temperate Land
Polar North
Polar South
Desert

b)

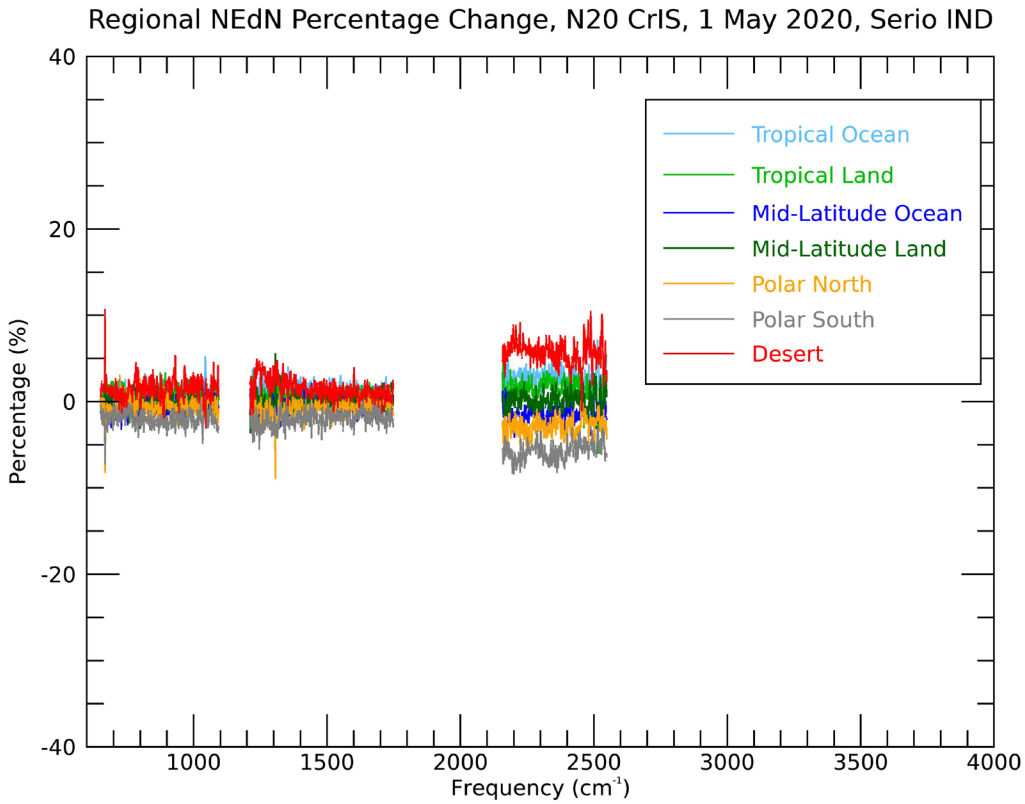

Figure 8: PCA noise change in percentage based on the 7 geographical regions wither respect to the global mean using the method 2 (a) and the method 3 with the IND criteria (b).

a)

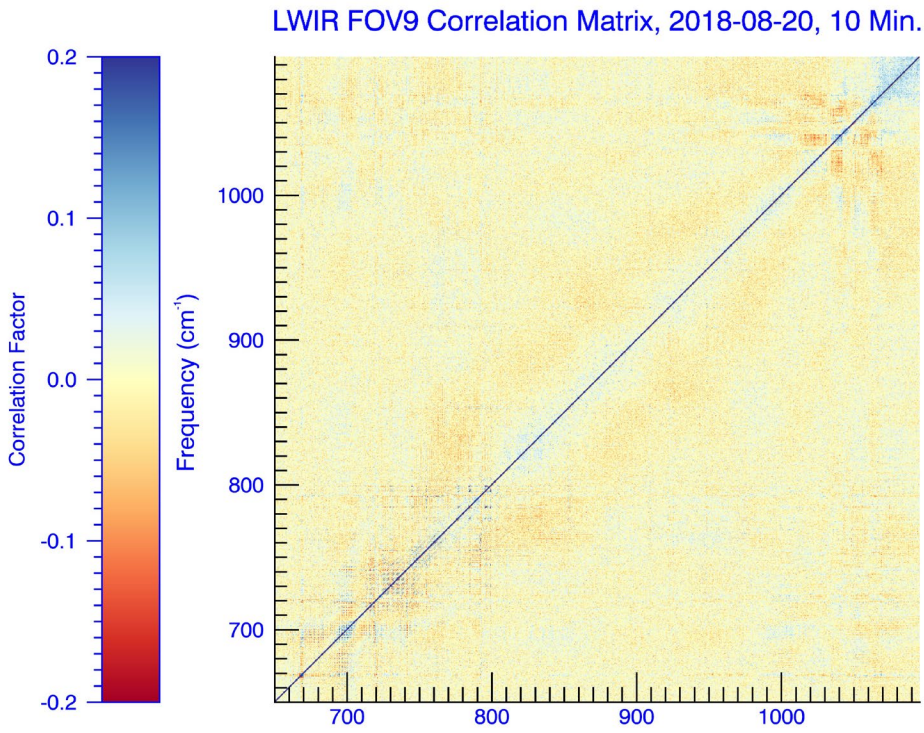
LWIR FOV9 Correlation Matrix, 2018-08-20, 10 Min.
Correlation Factor
0.2
0.1
0.0
-0.1
-0.2
Frequency (cm-1)
1000
900
800
700
700
800
900
1000

b)

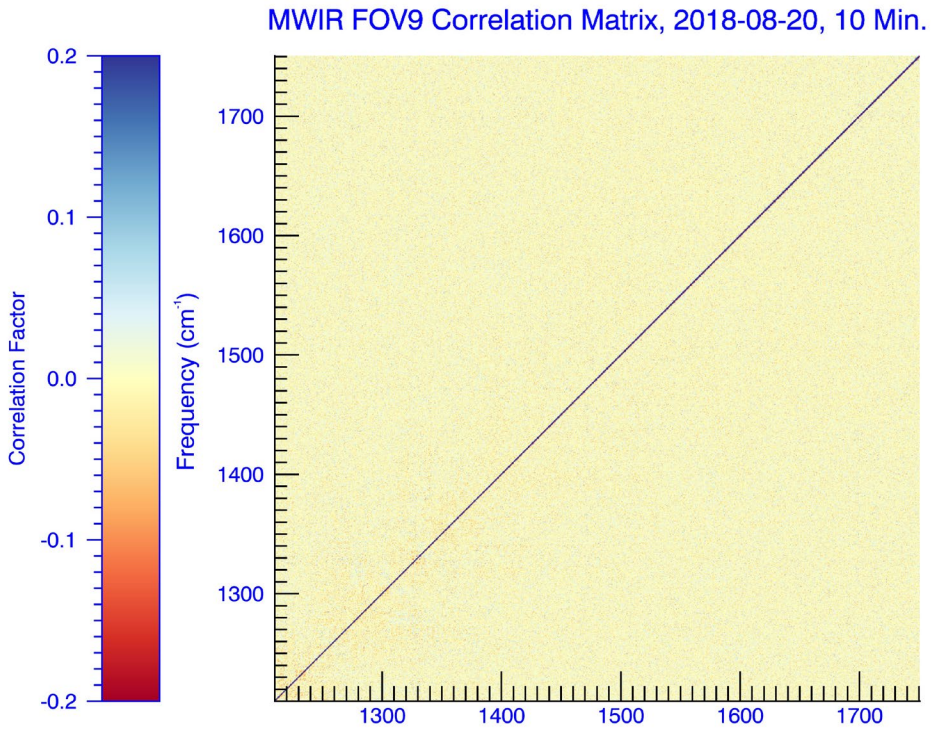
MWIR FOV9 Correlation Matrix, 2018-08-20, 10 Min.
Correlation Factor
0.2
0.1
0.0
-0.1
-0.2
Frequency (cm-1)
1700
1600
1500
1400
1300
1300
1400
1500
1600
1700

c)

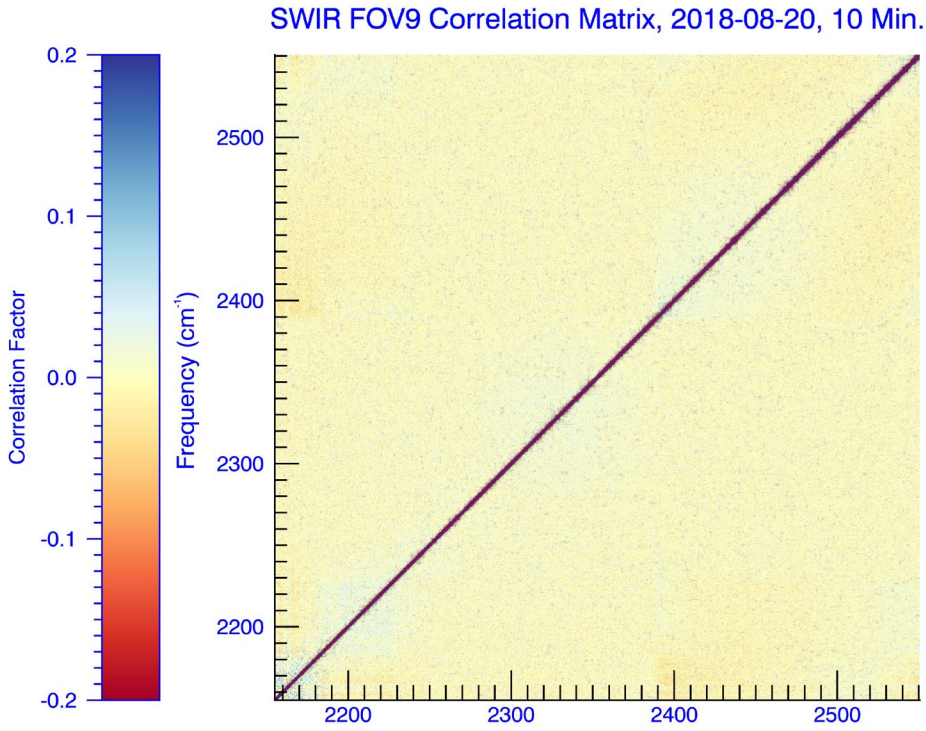
SWIR FOV9 Correlation Matrix, 2018-08-20, 10 Min.
Correlation Factor
0.2
0.1
0.0
-0.1
-0.2
Frequency (cm-1)
2500
2400
2300
2200
2200
2300
2400
2500

d)

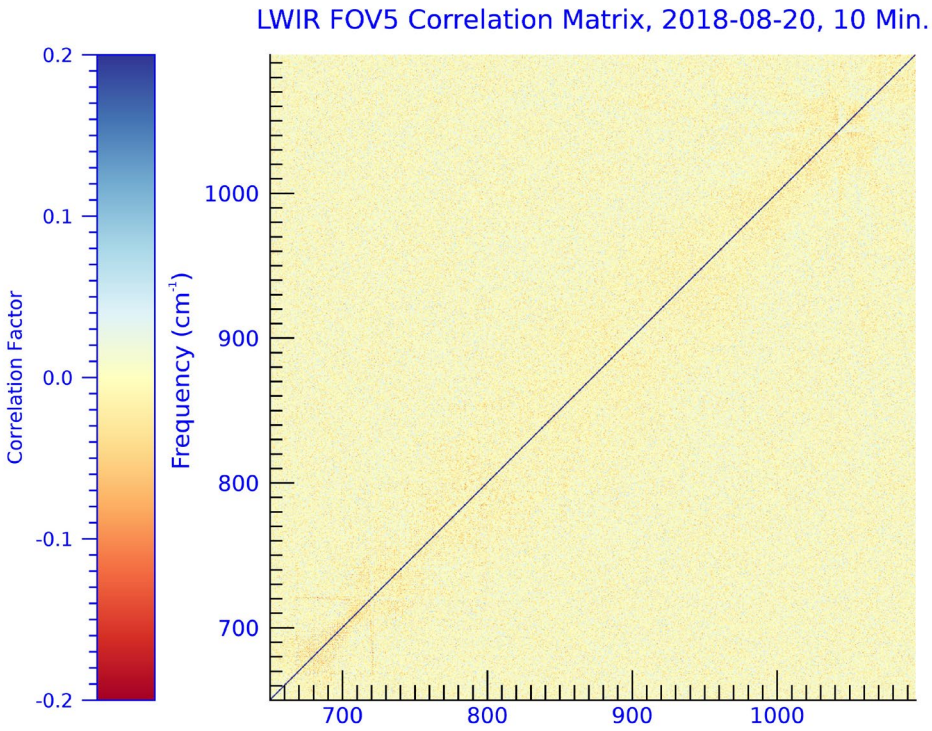

Figure 9: Full correlation matrix of FOV9 using the data set number 1 (10 minutes of data collection) on 20 August 2018 for LWIR (a), MWIR (b) , and SWIR (c) and for LWIR FOV5 (d).

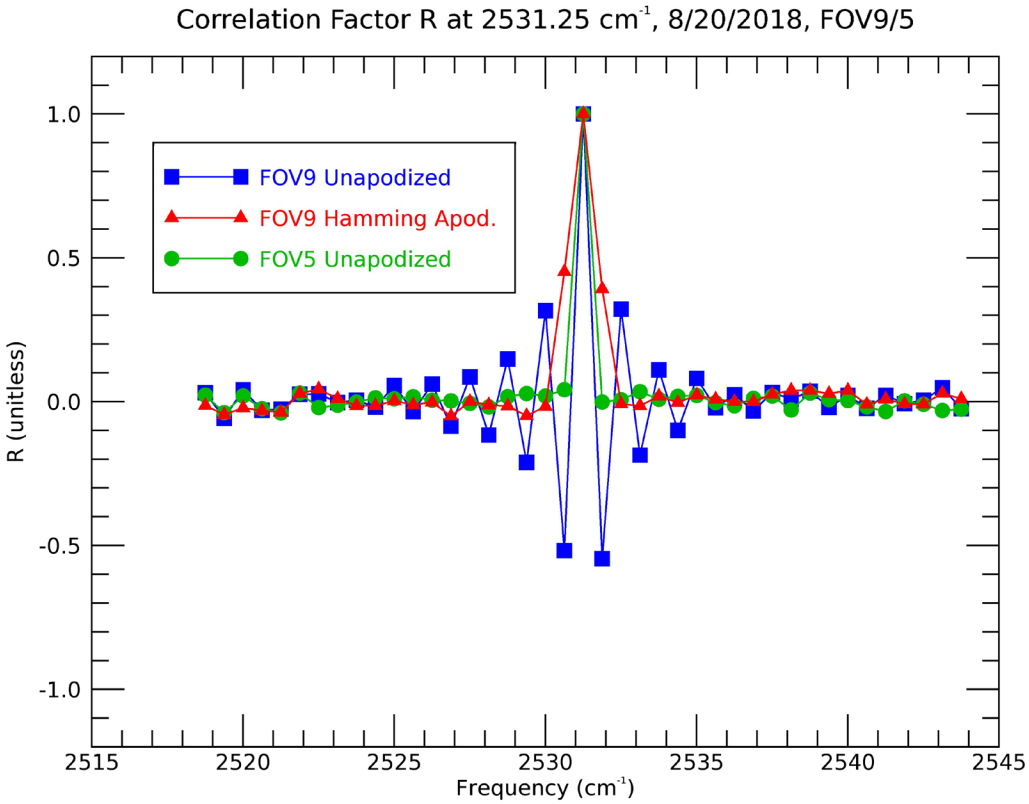

Figure 10: Correlation factor R about the frequency at 2531.25 cm-1 for SWIR FOV9 (unapodized and Hamming apodized) and FOV5 calculated from the 10 minutes data set number 1.

a)

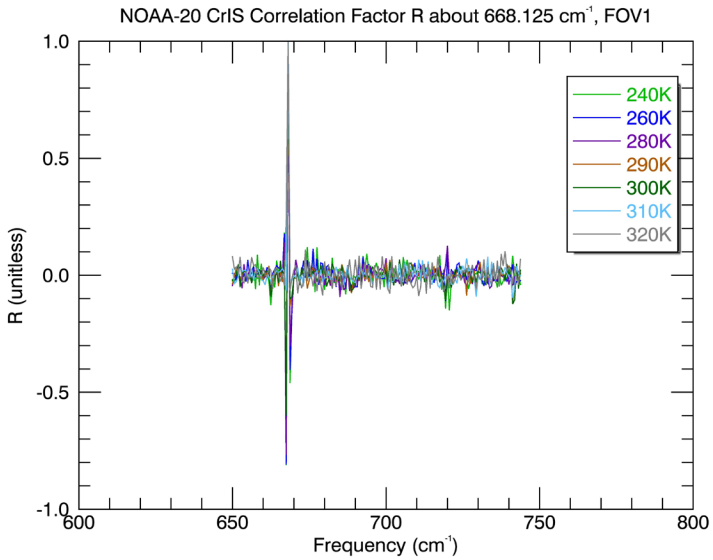

b)

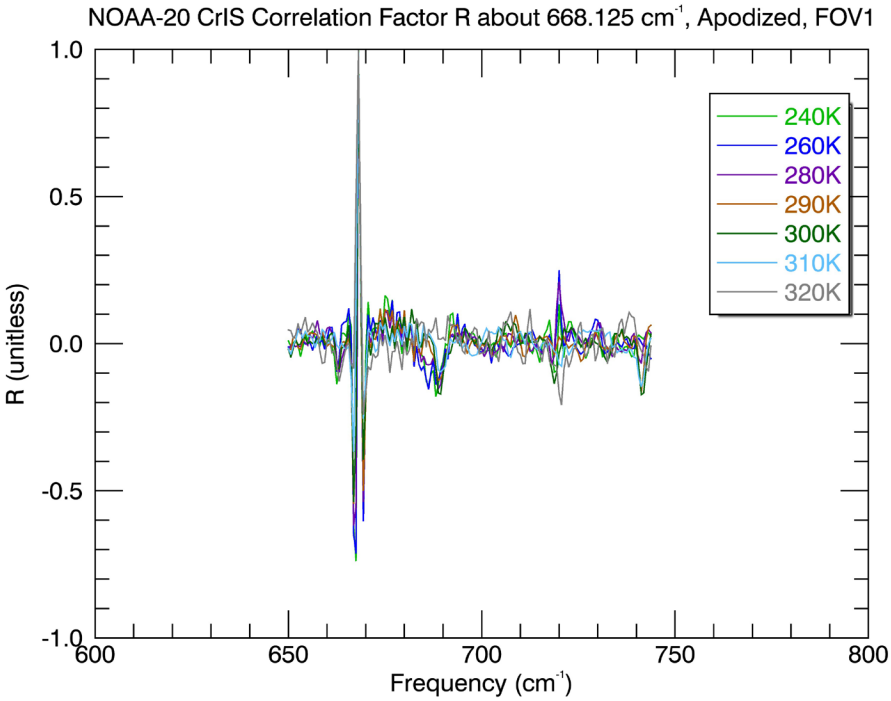

Figure 11: Correlation factor R of the 668.125 cm^{-1} frequency with respect to adjacent frequencies for unapodized (a) and Hamming apodized cases (b) using the binned BT data set using method 2.

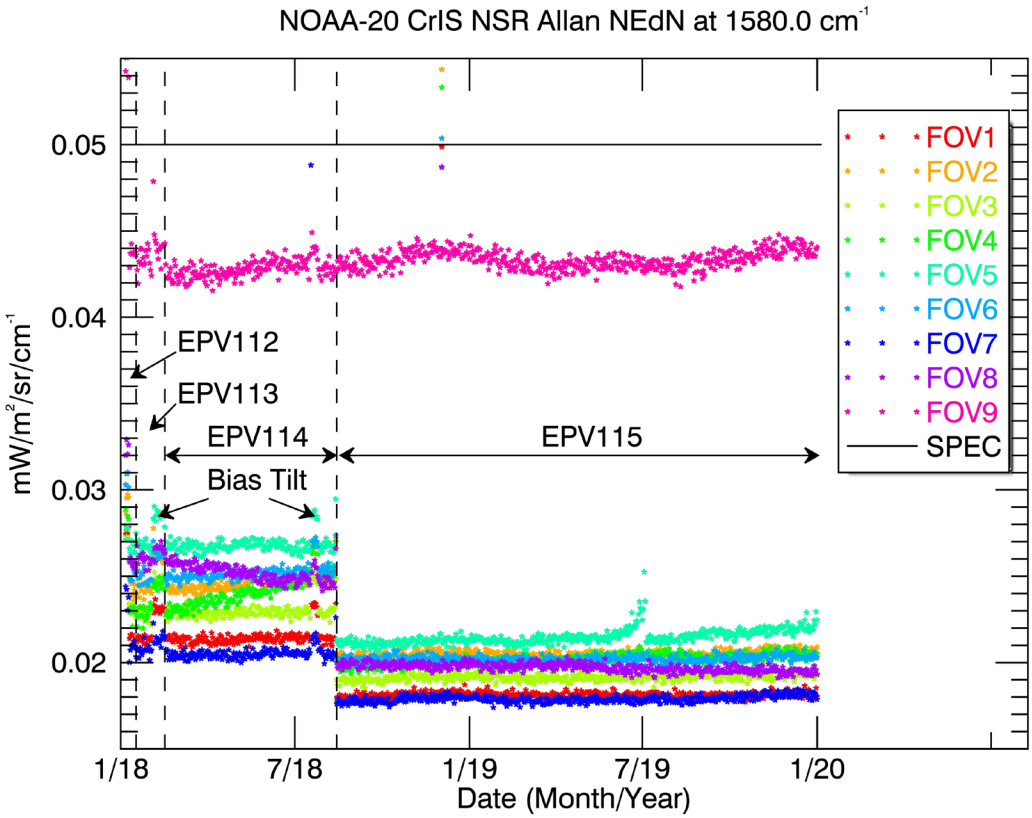

Figure 12: Time series of the Allan noise (method 4) at 1580 cm-1 frequency from 5 January 2018 to 31 December 2019 at nominal spectral resolution (NSR) with respect to the specification (black line).

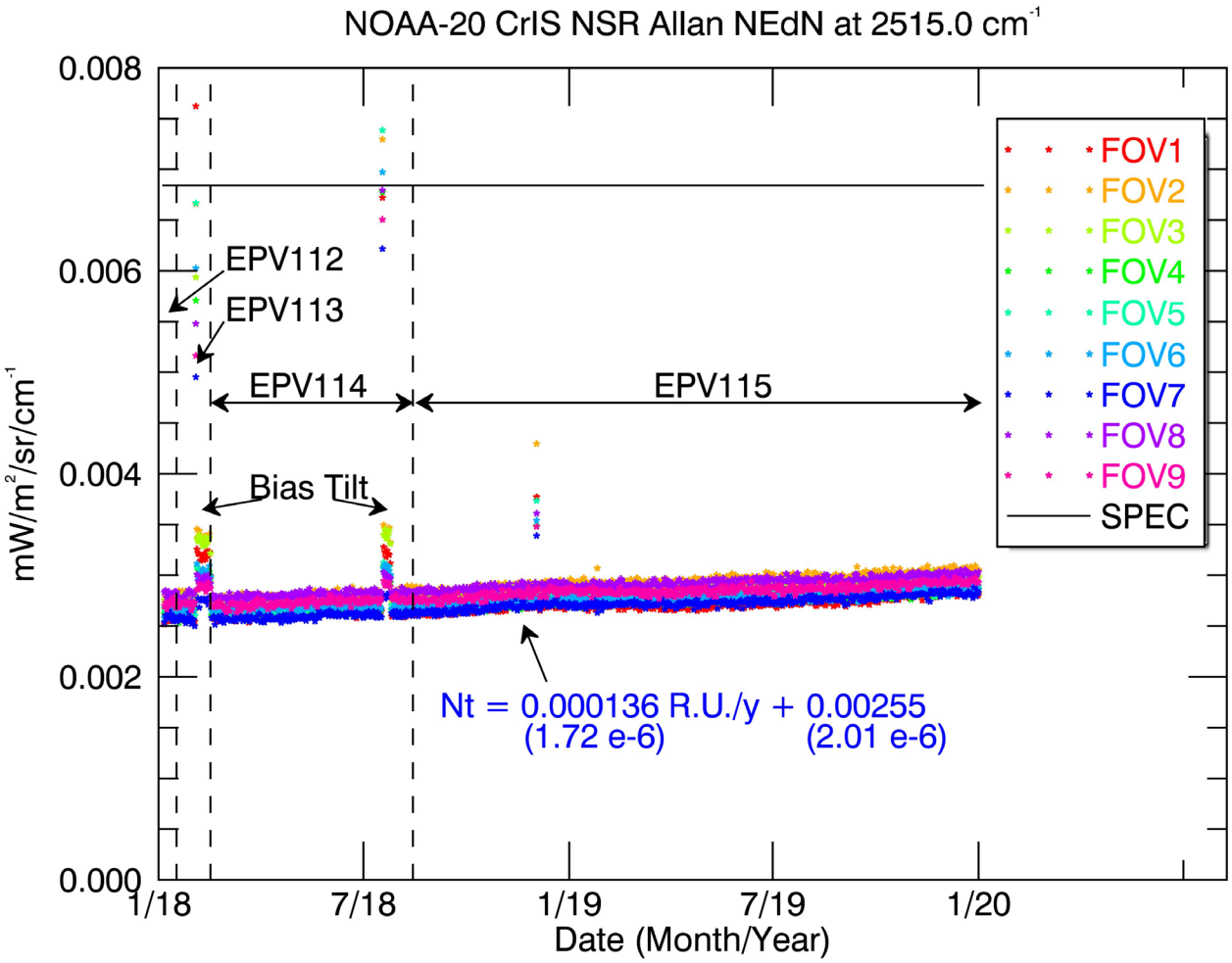

Figure 13: Time series of the Allan noise (method 4) at 2515 cm-1 frequency from 5 January 2018 to 31 December 2019. The yearly noise increase trend (Nt) is indicated for FOV7 along with the uncertainty for the slope and bias with respect to the specification (black line).

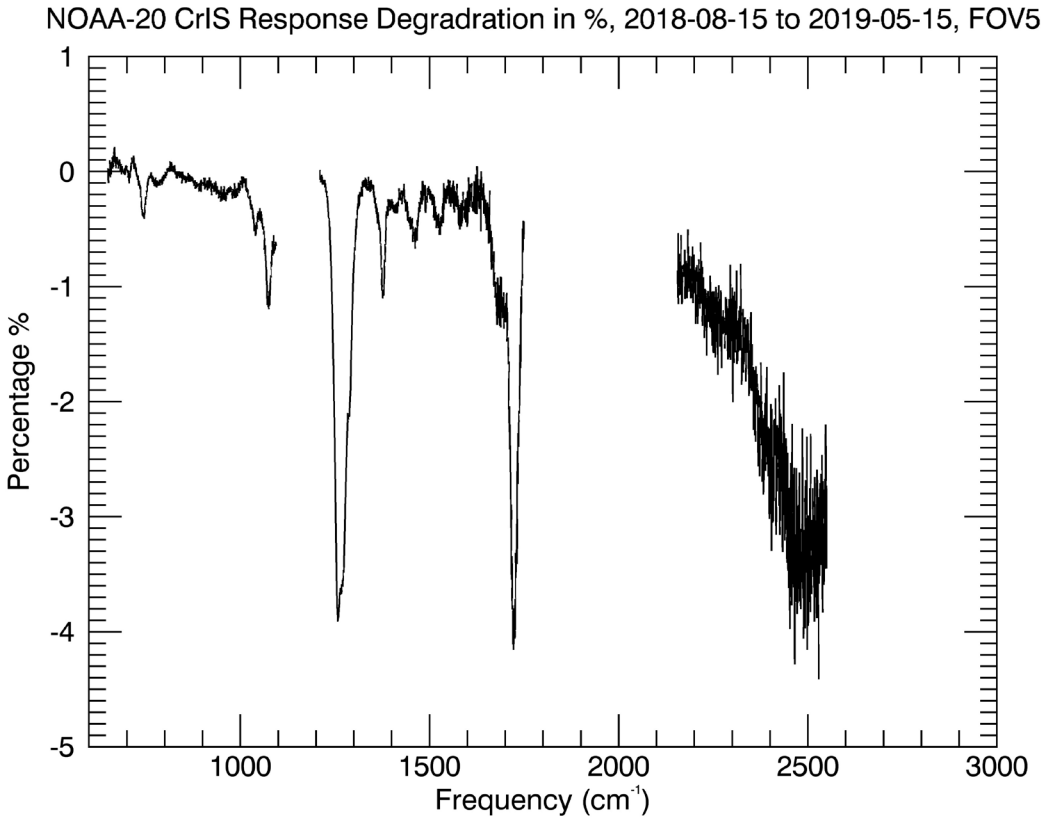

Figure 14: Absolute responsivity function degradation in percentage from 15 August 2018 to 15 May 2019 for FOV5.

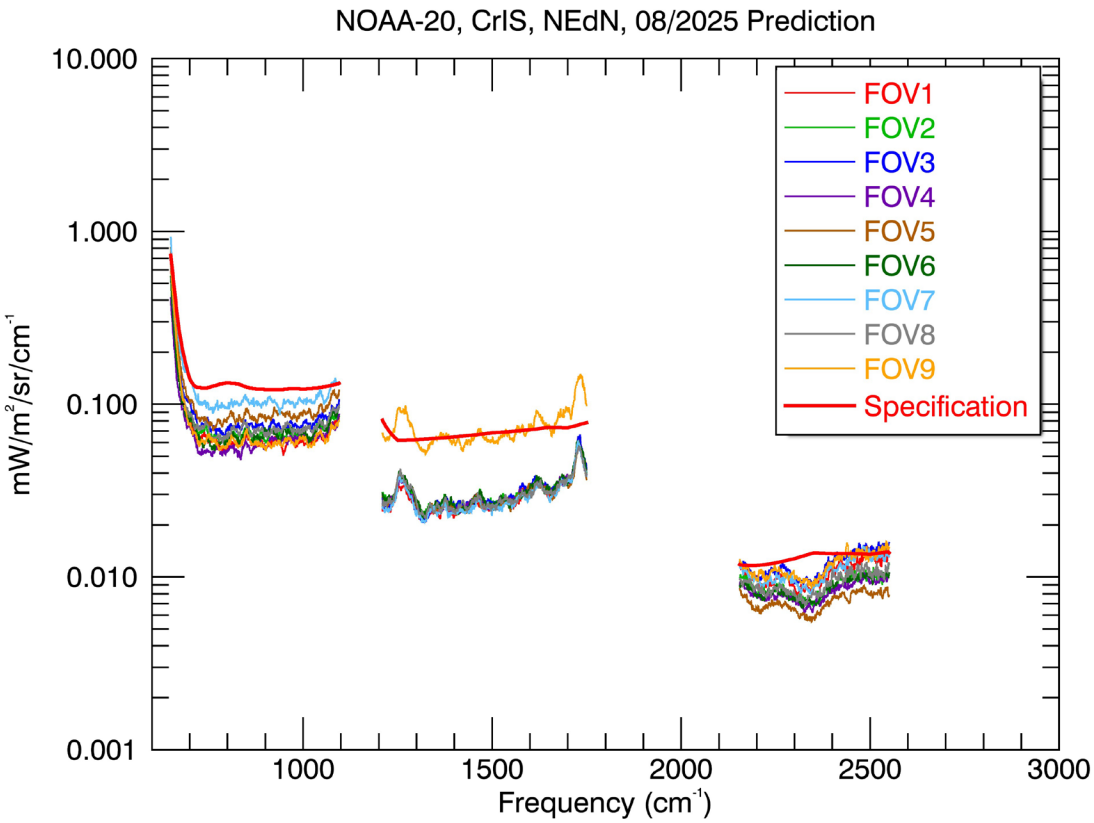

Figure 15: Predicted NEdN on August 2025.